Dynamics, Variability, and Change in Seasonal Precipitation Reconstructions for North America

DAVID W. STAHLE,[a] EDWARD R. COOK,[b] DORIAN J. BURNETTE,[c] MAX C. A. TORBENSON,[a] IAN M. HOWARD,[a] DANIEL GRIFFIN,[d] JOSE VILLANUEVA DIAZ,[e] BENJAMIN I. COOK,[f] A. PARK WILLIAMS,[b] EMMA WATSON,[g] DAVID J. SAUCHYN,[h] NEIL PEDERSON,[i] CONNIE A. WOODHOUSE,[j] GREGORY T. PEDERSON,[k] DAVID MEKO,[l] BETHANY COULTHARD,[m] AND CHRISTOPHER J. CRAWFORD[n]

[a] *Department of Geosciences, University of Arkansas, Fayetteville, Arkansas*
[b] *Lamont-Doherty Earth Observatory, Columbia University, Palisades, New York*
[c] *Department of Earth Sciences, University of Memphis, Memphis, Tennessee*
[d] *Department of Geography, University of Minnesota, Twin Cities, Minneapolis, Minnesota*
[e] *Centro Nacional de Investigacion Disciplinaria Relacion Agua-Suelo-Planta-Atmosfera, Lerdo, Mexico*
[f] *NASA Goddard Institute for Space Studies, New York, New York*
[g] *Environment and Climate Change Canada, Toronto, Ontario, Canada*
[h] *Department of Geography, University of Regina, Regina, Saskatchewan, Canada*
[i] *Harvard Forest, Petersham, Massachusetts*
[j] *School of Geography and Development, The University of Arizona, Tucson, Arizona*
[k] *U.S. Geological Survey, Bozeman, Montana*
[l] *Laboratory of Tree-Ring Research, The University of Arizona, Tucson, Arizona*
[m] *Department of Geosciences, University of Nevada, Las Vegas, Las Vegas, Nevada*
[n] *U.S. Geological Survey, Sioux Falls, South Dakota*

(Manuscript received 8 April 2019, in final form 3 January 2020)

ABSTRACT

Cool- and warm-season precipitation totals have been reconstructed on a gridded basis for North America using 439 tree-ring chronologies correlated with December–April totals and 547 different chronologies correlated with May–July totals. These discrete seasonal chronologies are not significantly correlated with the alternate season; the December–April reconstructions are skillful over most of the southern and western United States and north-central Mexico, and the May–July estimates have skill over most of the United States, southwestern Canada, and northeastern Mexico. Both the strong continent-wide El Niño–Southern Oscillation (ENSO) signal embedded in the cool-season reconstructions and the Arctic Oscillation signal registered by the warm-season estimates faithfully reproduce the sign, intensity, and spatial patterns of these ocean–atmospheric influences on North American precipitation as recorded with instrumental data. The reconstructions are included in the North American Seasonal Precipitation Atlas (NASPA) and provide insight into decadal droughts and pluvials. They indicate that the sixteenth-century megadrought, the most severe and sustained North American drought of the past 500 years, was the combined result of three distinct seasonal droughts, each bearing unique spatial patterns potentially associated with seasonal forcing from ENSO, the Arctic Oscillation, and the Atlantic multidecadal oscillation. Significant 200–500-yr-long trends toward increased precipitation have been detected in the cool- and warm-season reconstructions for eastern North America. These seasonal precipitation changes appear to be part of the positive moisture trend measured in other paleoclimate proxies for the eastern area that began as a result of natural forcing before the industrial revolution and may have recently been enhanced by anthropogenic climate change.

Supplemental information related to this paper is available at the Journals Online website: https://doi.org/10.1175/JCLI-D-19-0270.s1.

Corresponding author: David W. Stahle, dstahle@uark.edu

DOI: 10.1175/JCLI-D-19-0270.1

1. Introduction

The consequences of anthropogenic forcing to the global energy balance and regional land cover for climate dynamics, variability, and change over North America are a central focus of climate science and policy (USGCRP 2018). Because instrumental measurements of precipitation and temperature are too short to provide robust characterization of natural climate variability, questions surrounding the anthropogenic forcing of climate have stimulated over 50 years of paleoclimatic research to describe and analyze natural climate variability and change prior to the industrial revolution (e.g., Smerdon et al. 2017). The exactly dated, climate-sensitive, and spatially extensive tree-ring chronologies now available for North America have contributed to the reconstruction of preinstrumental climate (Cook et al. 1999, 2010a), particularly the history and dynamics involved in prolonged droughts and pluvials (Woodhouse et al. 2005; Cook et al. 2007; Seager et al. 2007).

The most severe and sustained droughts over North America during the instrumental era were the decadal scale extremes of the 1930s, 1950s, and early 2000s (Fye et al. 2003; Seager 2007). During the 1930s Dust Bowl and the 1950s southern Great Plains Drought, cool-season precipitation and temperature anomalies intensified during the warm season when land surface conditions appear to have amplified existing moisture anomalies associated with ocean–atmospheric forcing active in the cool season (Seager and Hoerling 2014). However, the rapid onset of ''flash droughts'' of 1980 and 2012 (Namias 1982; Mo and Lettenmaier 2015) and other less extreme spring-to-summer moisture reversals witnessed during the instrumental period document the large uncertainty involved in anticipating warm-season moisture levels based on antecedent conditions during the cool season. This observed variability in seasonal moisture anomalies over North America has motivated the development of long tree-ring chronologies that are well correlated with either cool- or warm-season moisture, but not with both, in order to extend the limited instrumental observations of seasonal persistence and change deeper into the preinstrumental era (Stahle et al. 2009; Griffin et al. 2013). These seasonally discrete tree-ring proxies do exist in some numbers, but they have not been employed in systematic gridded reconstructions of both cool- and warm-season precipitation totals at the continental scale. This article describes the development of cool- and warm-season precipitation reconstructions for North America and then uses the reconstructions to investigate the climate dynamics, variability, and long-term changes registered in the seasonal estimates over the past several hundred years.

Most North America tree-ring chronologies are sensitive to the long-term soil moisture balance. However, the over 2500 North American tree-ring chronologies include a subset of chronologies that are correlated with winter–early spring precipitation and another subset that is sensitive to late spring–midsummer rainfall, but not both. We have identified these separate tree-ring chronology predictors of cool- and warm-season precipitation to reconstruct December–April (DJFMA) and May–July (MJJ) precipitation totals on a 0.5° latitude/longitude grid over most of North America. The DJFMA cool season and MMJ warm season are the specific months most highly correlated with the moisture response of most available North American tree-ring chronologies that have a distinct seasonal signal. For brevity we refer to these dendroclimatic seasons as the ''cool'' or ''warm'' season, but these bioclimatic subdivisions do differ slightly from the standard 3-month seasons [December–February (DJF), March–May (MAM), June–August (JJA), and September–November (SON)]. The gridded reconstructions are referred to as the North American Seasonal Precipitation Atlas (NASPA). The NASPA seasonal reconstructions calibrate at least 40% of the instrumental precipitation variance over most of North America, extend back over certain regions from 500 to 2000 years, and provide a new perspective on cool- and warm-season climate variability and change. These tree-ring estimates of precipitation faithfully record important ocean–atmospheric circulation forcing of cool- and warm-season precipitation over North America witnessed in the instrumental observations, provide estimates of the seasonal nature of major droughts and pluvials during the preinstrumental period, and identify statistically significant centennial-scale trend in cool- and warm-season precipitation over subregions of North America.

2. Seasonal moisture signal in North American tree rings

Over 2500 well-dated, climate-sensitive tree-ring chronologies are now available for North America, many of which have been contributed to the International Tree-Ring Data Bank (ITRDB) hosted at the paleoclimatology archive of the NOAA National Centers for Environmental Information for open access by the scientific community (Grissino-Mayer and Fritts 1997). A diversity of seasonal climate signals are encoded in these proxy tree-ring chronologies, including positive correlations with warm-season rainfall (e.g., Schulman 1942; Cleaveland 1986; Therrell et al. 2002; Griffin et al. 2013; Torbenson and Stahle 2018), strong positive response to cool-season precipitation that recharges the soil moisture

column prior to the growing season (e.g., Fritts 1966; Villanueva-Diaz et al. 2007; Stahle et al. 2009), a negative winter precipitation correlation in the Pacific Northwest that is due to deep snowpack inhibition of spring–early summer tree growth (Pederson et al. 2011; Welsh et al. 2019), and in certain narrow alpine tree line positions even a positive correlation with mean monthly temperature during the summer period of high-elevation tree growth (e.g., Salzer et al. 2014). Most of these tree-ring chronologies have been previously used to develop the North American Drought Atlas (NADA; Cook et al. 2004), where a point-by-point regression (PPR; Cook et al. 1999) procedure was used to reconstruct the summer (JJA) Palmer drought severity index (PDSI; Palmer 1965) at each of 11 396 grid points with a resolution of 0.5° across the continent (Cook et al. 2010a).

The summer PDSI reconstructed for the NADA provides a high-quality estimate of the long-term soil moisture balance conditions that advance or constrain tree growth in most natural forests across North America. The NADA summer PDSI reconstructions have been used to reproduce the detailed temporal and spatial history of continent-wide soil moisture conditions for the past 1000 years, and for the past 2000 years over portions of the continent where the oldest moisture-sensitive trees are found. The NADA has been used extensively for analysis of climate variability and change (e.g., Fye et al. 2003; Herweijer et al. 2006; E. R. Cook et al. 2010a, 2014), investigation of the underlying climate dynamics responsible for moisture variability over North America (B. I. Cook et al. 2014; Coats et al. 2016; Baek et al. 2017), exploration of the role of climate in fire and ecosystem dynamics (Swetnam et al. 2009; Marlon et al. 2017), and exploration of the impacts of climate on ancient and modern societies (e.g., Benson et al. 2009; Stahle and Dean 2011; Burns et al. 2014).

Because of the strong month-to-month persistence built into the PDSI formulation to model the slow accumulation and depletion of soil moisture (Palmer 1965; Cook et al. 2007), the PDSI in a given month represents the integration of precipitation inputs and evaporative losses over the course of approximately one year. Because many tree-ring chronologies from North America integrate climate and soil moisture conditions for several months during and preceding the growing season, the PDSI is an excellent index of the slowly evolving hydroclimate conditions that frequently drive tree growth. However, many North American tree-ring chronologies have a more restricted monthly moisture signal and can be used to estimate seasonal-scale changes in climate (Meko and Baisan 2001; Stahle et al. 2009; St. George 2014). For example, time series of blue oak growth in the Mediterranean climate of California have a strong correlation with winter–spring precipitation [e.g., November–April, Meko et al. (2011); September–May; Stahle et al. (2013)], while some forest species in the eastern United States are only correlated with late spring and summer moisture levels, especially MJJ (e.g., Cook and Jacoby 1977; Elliott et al. 2015; LeBlanc and Stahle 2015). Many conifer and hardwood species also form well-defined spring and summer growth bands (i.e., earlywood and latewood; Fig. 1) that can be readily identified and separately measured to produce subannual chronologies of earlywood and latewood width that can have discrete seasonal climate signals (e.g., Schulman 1942; Meko and Baisan 2001; Griffin et al. 2013; Torbenson and Stahle 2018; Howard and Stahle 2020).

To develop the NASPA, all available tree-ring chronologies in Canada (south of 60°N), the United States, Mexico, and western Guatemala were screened for ''discrete correlation'' with precipitation totals for each season using the Global Precipitation Climatology Centre (GPCC) gridded 0.5° monthly precipitation totals (Becker et al. 2013). Discrete correlation is used here to identify chronologies with a significant precipitation correlation during one season but no significant correlation with the alternate season ($p < 0.05$). Unlike the PDSI, monthly or seasonal precipitation totals do not tend to be strongly correlated and can therefore represent the discrete seasonal hydroclimate conditions that drive tree growth. The two subsets of tree-ring chronologies with discrete seasonal precipitation signals were used to develop separate cool-season (DJFMA) and warm-season (MJJ) precipitation reconstructions for most of North America during the Common Era. Because the correlations between the gridded cool- and warm-season precipitation reconstructions are still higher in some areas than observed in the instrumental precipitation data, a third set of gridded reconstructions of MJJ precipitation was produced. This was accomplished by using linear regression, grid point by grid point, to remove the antecedent cool-season precipitation signal from the warm-season reconstructions for the period 1400–2016, thus producing the so-called persistence-free MJJ reconstructions (MJJpf). All three gridded reconstructions (DJFMA, MJJ, and MJJpf), along with the seasonal GPCC precipitation data, are provided, and can be investigated, online (http://drought.memphis.edu/NASPA).

This article presents the DJFMA and the MJJpf reconstructions, but additional analyses of the MJJ

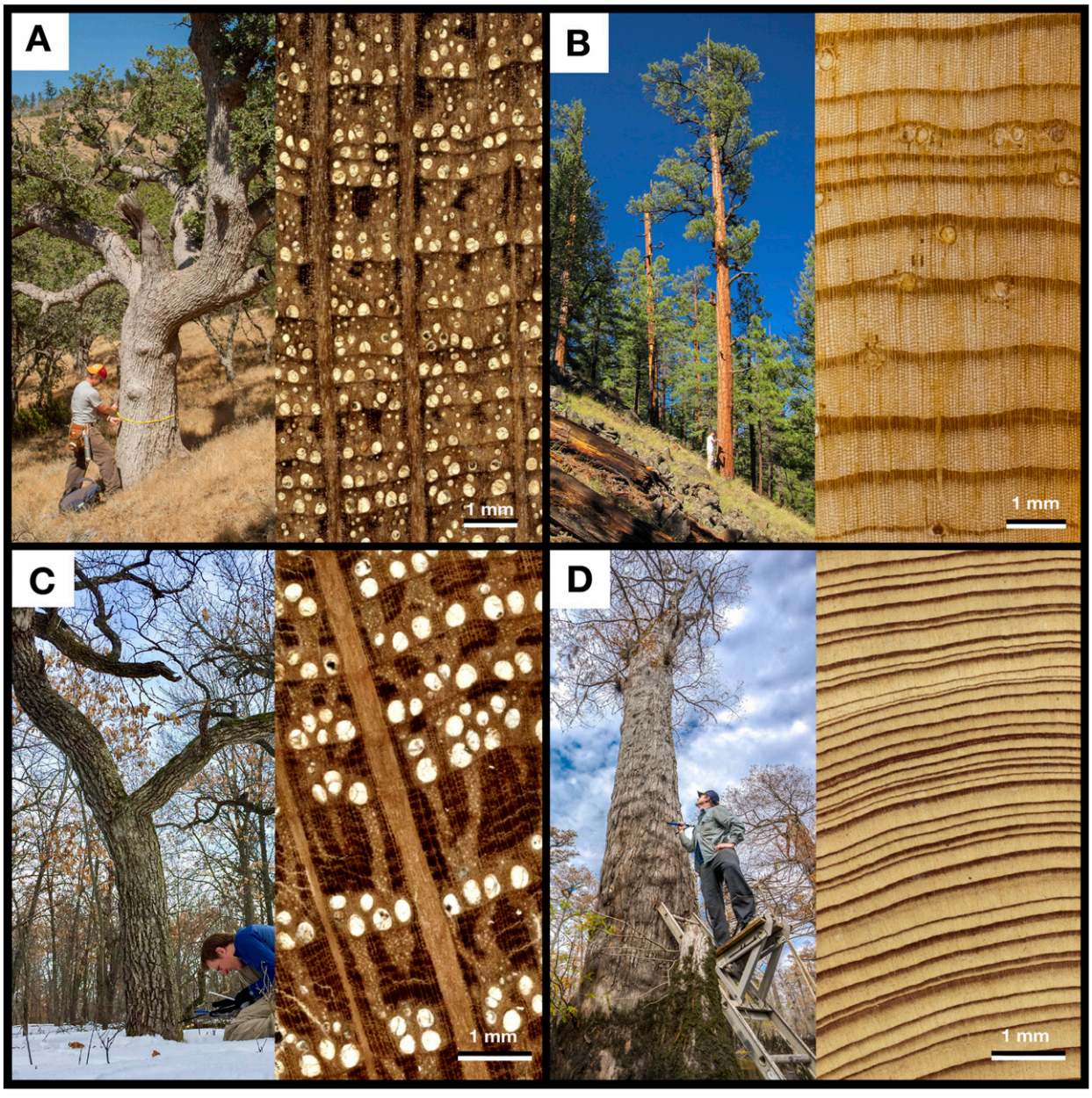

FIG. 1. Four important tree species for seasonal precipitation reconstruction are illustrated, along with photomicrographs of their annual rings that display prominent variability in earlywood and latewood width: (a) blue oak (*Quercus douglasii*), (b) ponderosa pine (*Pinus ponderosa*), (c) bur oak (*Q. macrocarpa*), and (d) bald cypress (*Taxodium distichum*).

precipitation estimates are presented in the supplemental material.

3. Methods

a. Instrumental precipitation data

The Global Precipitation Climatology Center Full Dataset (GPCC_FD) gridded monthly precipitation estimates extending from 1891 to 2016 were used to calibrate and validate the NASPA (ftp://ftp.dwd.de/pub/data/gpcc/html/fulldata-monthly_v2018_doi_download.html; Becker et al. 2013; Schneider et al. 2018). At each 0.5° grid point on land between 14° and 55°N and between 50° and 135°W the precipitation data were totaled for the DJFMA cool season and the MJJ warm season. Correlation analyses indicate that these seasons optimize the seasonal precipitation signals in the available North American tree-ring data. The seasonal reconstructions were based on power

transformed GPCC precipitation data using the method of Hinkley (1977) in order to symmetrize the distribution to quasi normality before using principal components regression (described below). After computing the reconstructions the power-transformed precipitation estimates at each grid point were inverse-transformed back to the original units of precipitation (mm). The instrumental and reconstructed precipitation totals were then transformed into the standardized precipitation index (SPI; Guttman 1999) to facilitate the mapping of seasonal precipitation anomalies.

Computing the SPI involved fitting gamma distributions to the cool- and warm-season precipitation data at each grid point. The parameters of the gamma distribution were derived using L-moments, which are analogous to traditional moments but tend to be more robust estimates of summary statistics for probability distributions (Hosking 1990; Guttman et al. 1993). The calculation of these gamma distribution parameters was based on the period 1860–2016, using the reconstructed precipitation data from 1860 to 1978 and the instrumental data from 1979 to 2016. The same estimated parameters were then used to compute the gamma probabilities for both the instrumental and reconstructed data at each grid point, but because gamma is undefined for precipitation values equal to zero, a modification to the cumulative probability was warranted:

$$H(x) = q + (1 - q)G(x),$$

where $G(x)$ are the original gamma probabilities, q is the probability of a zero, and $H(x)$ are the final gamma probabilities. Thom (1966) notes that q can be estimated by summing the number of zeroes encountered and dividing by the number of precipitation values, and this method was followed. The final cumulative probabilities $H(x)$ at each grid point were then transformed into standard normal random variables Z. These values for Z were the final SPI values (Edwards and McKee 1997).

The monthly precipitation estimates extend back to 1891 at all grid points, but in regions with few station observations the GPCC estimates relax to monthly climatology (Becker et al. 2013), most notably before 1920 (e.g., Fig. SM-1 in the online supplemental material). For this reason, the NASPA was calibrated with the seasonal GPCC during the 1928–78 data-rich interval in common with most available tree-ring chronologies. Note that many chronologies end in the last quarter of the twentieth century when the tree-ring samples were collected. The NASPA reconstructions were then validated from 1901 to 1927, excluding the last decade of the nineteenth century when the GPCC estimates are most limited over portions of Canada, the western United States, and Mexico. The few station observations during the early-twentieth century seen in Fig. 2 very likely degrade the statistical validation of the seasonal precipitation reconstructions in some areas, but as discussed below there is strong evidence for the validity of the tree-ring estimates over much of the continent in spite of weak validation statistics in some areas during the 1901–27 validation period. In fact, the tree-ring reconstructions in the NASPA may provide more accurate estimates of seasonal precipitation during the late-nineteenth and early-twentieth century in data-poor regions such as Sonora, Mexico (online supplemental Fig. SM-1), than is available in the GPCC or any other gridded instrumental precipitation products.

Experimental reconstructions of seasonal precipitation were also developed using the Climatic Research Unit monthly precipitation totals (CRU TS4.021; Harris et al. 2014). These CRU-based reconstructions used a similar but not identical subset of North American tree-ring chronologies with discrete seasonal precipitation signals, and the derived reconstructions are similar to those produced using the GPCC data. In fact, because the CRU seasonal precipitation estimates tend to be more spatially smoothed than the GPCC estimates, the calibration and validation results were higher in some regions than those observed when calibrating with the GPCC. Nonetheless, the GPCC was selected for the final reconstructions because of the much larger number of station observations used to compute the gridded monthly estimates (Becker et al. 2013) and the more detailed spatial resolution of the monthly and seasonal precipitation totals.

b. *Selection of tree-ring chronologies with discrete seasonal moisture signals*

The exact monthly to seasonal moisture response of tree-ring chronologies varies across North America due to phenological development associated with the "march of the seasons," spatial differences in the seasonal distribution of precipitation, and many other species and stand level precipitation response factors (e.g., Fritts 1976; Cook et al. 1999). But some chronologies are correlated mainly with cool-season precipitation (DJFMA), and another separate subset is mainly correlated with warm-season precipitation (MJJ). Screening was performed to identify the maximum number of tree-ring chronologies in each seasonal subset, using correlation analysis between the candidate chronologies and the DJFMA and MJJ precipitation totals (Torbenson 2019). These seasons differ by one month from the traditional climatological definition of winter–spring

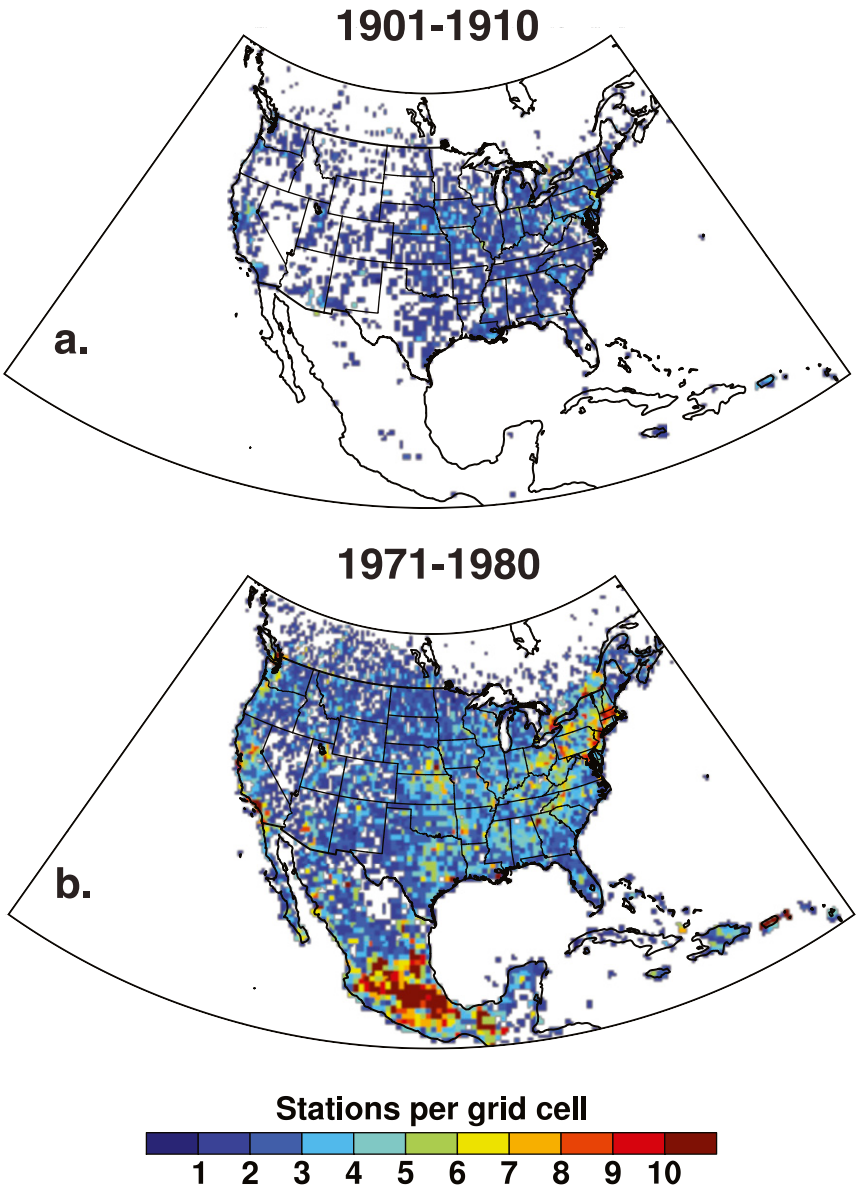

FIG. 2. The availability of instrumental precipitation measurements in the GPCC Full Dataset is illustrated for two decades in the early- and late-twentieth century by the median number of stations per 0.25° grid cell.

(DJF–MAM) and summer (JJA) because May moisture can be important to the growth of trees primarily correlated with the cool season, and for other trees mainly correlated with the warm season. Nonetheless, the May moisture response appears to be most commonly associated with warm-season-sensitive tree-ring chronologies and was therefore included with June and July to represent the warm season in the NASPA reconstructions.

The precise screening procedure used to identify the cool- and warm-season predictors involved computing the Spearman rank correlation coefficient for all available tree-ring chronologies from North America (i.e., 14°–60°N) with DJFMA and MJJ total precipitation at the nine grid points closest to each chronology for the 1928–78 calibration period. The discretion test was then based on the single grid point of the nine closest that was most highly correlated for the target season for the over 2500 tree-ring chronologies. For sites that included total ring width (RW), earlywood width (EW), latewood width (LW), and adjusted LW width chronologies (i.e., LW_a; Meko and Baisan 2001), only the chronology that

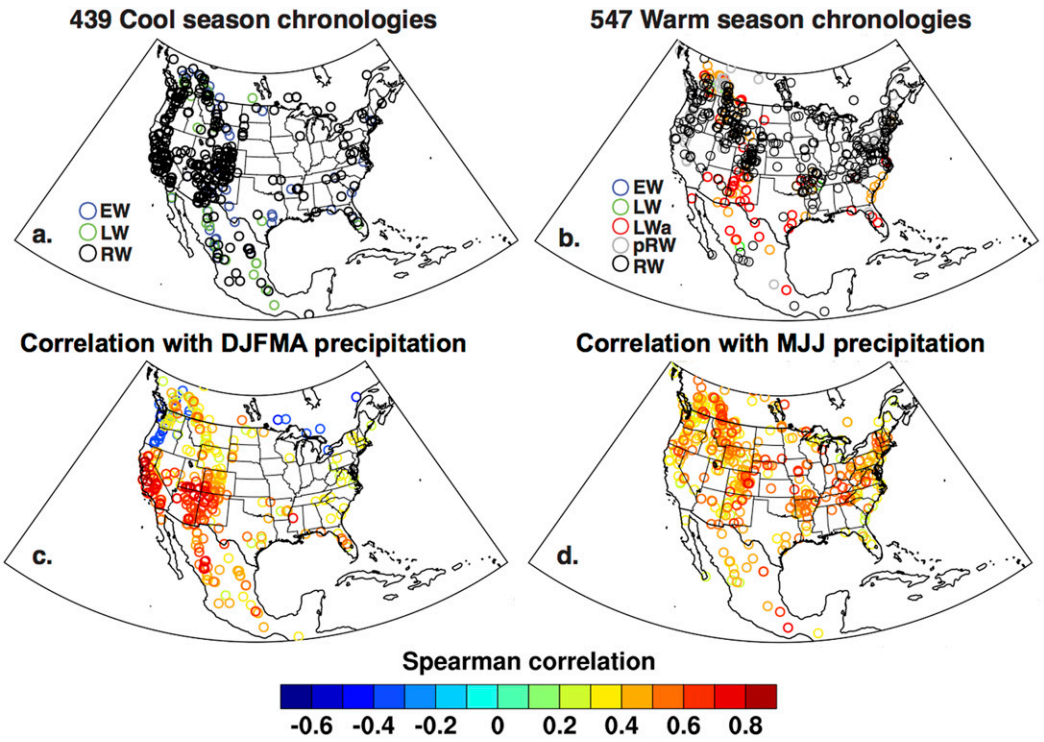

FIG. 3. Site locations for (a) the 439 tree-ring chronologies that are discretely correlated with cool-season precipitation (DJFMA), and (b) the 547 chronologies discretely correlate with warm-season totals (MJJ). The type of chronology used is also indicated (EW is earlywood; LW is latewood; LW*a* is adjusted latewood; RW is total ring width; *p*RW is ring width with a prior-year warm-season signal). The Spearman rank-order correlation computed between each chronology and the nearest GPCC precipitation grid point is mapped for (c) DJFMA and (d) MJJ totals.

displayed the strongest correlation with precipitation was chosen for either season. Chronologies that were significantly correlated with DJFMA precipitation ($p < 0.05$), but were not significantly correlated with MJJ precipitation ($p > 0.05$), were then selected as discrete candidate predictors of cool-season moisture. Those significantly correlated only with MJJ were selected as candidate predictors of the warm-season precipitation totals. Only EW and LW (or LW_a) chronologies from the same site could be selected for different seasons (e.g., a LW chronology could not be selected for the warm season if the RW chronology was used for the cool season).

Using this screening approach, 439 North American tree-ring chronologies were identified with a discrete cool-season signal and 547 were identified with a separate warm-season response (Fig. 3). This objective screening for discrete seasonal predictors was designed to produce two reconstructions, cool- and warm-season estimates of precipitation across North America useful for investigation of seasonal hydroclimate variability and large-scale climate dynamics. The screening was also intended to produce reconstructions that mimic the magnitude and spatial patterns of persistence between cool- and warm-season moisture witnessed in instrumental precipitation for North America. This screening minimized the interseasonal correlation in the derived reconstructions due to biological growth persistence, which can be inherently strong in subannual chronologies of EW and LW width drawn from the same trees (Torbenson et al. 2016). However, the spatial distribution of selected cool- and warm-season chronologies clearly differs (Fig. 3). The cool-season chronologies are strongly concentrated in western North America where winter season soil moisture recharge is most important to growth. In comparison, the warm-season chronologies are more uniformly distributed across the continent and reflect those sites and species that are more reliant on the delivery of moisture during the growing season. These spatial limitations of the seasonal proxies have had an important impact on the fidelity of the reconstructions in data-sparse regions.

c. *Tree-ring chronology development*

Once the chronologies with discrete seasonal moisture signals were identified using standardized tree-ring

series, the raw ring-width data for the selected series were reprocessed to produce ring-width chronologies that preserve common high and medium frequency variance (i.e., from interannual to multidecadal). The raw ring-width data for each measured radius were detrended and standardized using the signal free method (Melvin and Briffa 2008; Cook et al. 2015). The raw ring-width data were not available for some sites so the standardized ring-width chronologies were used for those sites (i.e., 35 of 439 for the cool season and 47 of 547 for the warm season). The sample size varies for each tree-ring chronology, but most chronologies used in the NASPA are based on exactly dated and precisely measured radii from 20 to over 40 trees per site. An age-dependent spline function (Melvin et al. 2007) was fit empirically to each dated and measured radial series, where the stiffness of the spline increases with the age of the tree and in the process tracks the observed trajectory of radial growth more naturally compared to the modified negative exponential curve (Fritts et al. 1969).

To reduce bias in the detrended and standardized ring-width indices, the raw ring widths were first power transformed and the indices were calculated by subtraction of the fitted curve value from the measurement value for each year in the time series (Cook and Peters 1997). The biweight robust mean value function (Hoaglin et al. 2000) was then used to compute the mean index tree-ring chronology from the individually detrended and standardized time series from all available trees and radii at each site. Long-term trends in variance of the final signal free chronology were sometimes present due to nonclimatic factors such as changes in sample size of dated radii and the loss of ring-width variance in some very old trees. Consequently, the variance of the signal free chronologies was detrended (i.e., stabilized) by fitting an age-based spline to the absolute values of the chronology, subtracting the fitted and observed values per year, and restoring the sign of the chronology (Meko et al. 1993). The discrete tree-ring chronologies vary from 160 to 2000 years in length. Based on the number and spatial distribution of predictor tree-ring chronologies (online supplemental Fig. SM-2; Fig. 2), the sample size is likely adequate for the seasonal precipitation reconstructions over most of North America from 1400 to 2016.

d. Gridded cool- and warm-season precipitation reconstructions

Point-by-point regression (Cook et al. 1999, 2010a) was used to develop reconstructions of the cool- and warm-season precipitation totals at each of 6812 0.5° grid points over southern Canada, the conterminous United States, and Mexico. PPR involves the fitting of principal components regression (PCR) models based on the tree-ring chronologies located within a given search radius around each grid point of instrumental precipitation data, under the assumption that the chronologies located in the vicinity of each grid point will covary with precipitation at that point in a direct and stable manner (Cook et al. 1999). Tree-ring chronologies with a discrete cool or warm-season moisture signal in North America were considered for these reconstructions. The instrumental precipitation totals extend from 1891 to 2016, but many tree-ring chronologies were collected much earlier and end in the late 1970s or 1980s. The time interval from 1928 to 1978 was used as the calibration period since it was common to all selected tree-ring chronologies and the instrumental precipitation totals. The instrumental precipitation data available from 1901 to 1927 were withheld for independent validation of the reconstructions, including Shoemaker F tests for the equality of variance between the instrumental and reconstructed precipitation totals (Shoemaker 2003; online supplemental Fig. SM-3). The validation interval was not used to screen for discrete seasonal correlation. These calibration and validation periods are similar to those used to produce the NADA [Cook et al. (2004) used 1928–78 and 1900–27].

The reconstructions were computed with a correlation-weighted, ensemble-based version of PPR first developed for the Monsoon Asia Drought Atlas (Cook et al. 2010b). There were 16 total ensemble reconstructions for each season: 8 ensemble members using predictors from within a 500-km search radius around each instrumental precipitation grid point and 8 more ensemble members using predictors from within a 1000-km search radius. The 500-km search radius approximates the correlation decay length defined by the e-folding level of correlation ($1/e$) between precipitation grid points (New et al. 2000; Mitchell and Jones 2005). The 1000-km search radius allows for the registration of large-scale droughts and pluvials in the seasonal tree-ring proxies, and the relatively sparse and irregular distribution of the tree-ring networks used for seasonal precipitation reconstruction on a regular 0.5° grid (see Fig. 3). Because the tree-ring chronologies located by the 1000-km search radius include those in the 500-km search radius, the ensemble average is heavily weighted by the 500-km tree-ring series used. For separate cool- and warm-season precipitation reconstruction, these large search radii are needed to identify discrete seasonal tree-ring predictors. They also contribute to the spatial smoothing of the reconstructions, however.

The PPR ensemble method incorporates the covariance between the tree-ring chronologies and the climate target variable by first weighting each tree-ring chronology by some power of its correlation over the calibration period with the climate variable being reconstructed (Cook et al. 2010b, 2013). This is expressed as

$$w\mathrm{TR} = u\mathrm{TR}_{*}r^{p},$$

where uTR is the unweighted tree-ring chronology in normalized $N[0, 1]$ form over the calibration period, r is its calibration period absolute correlation with the climate variable being reconstructed, p is a power weighting applied to r, and wTR is the resulting correlation-weighted chronology. This weighting method thus transforms the correlation matrix of tree-ring predictors into a covariance matrix that emphasizes the more heavily weighted (better correlated with climate) tree-ring series. PCR is then conducted using this correlation-weighted covariance matrix. See Cook et al. (2010b) for its first use in drought atlas development.

There is no a priori reason why any particular power weighting, p, should be optimal. Thus, a range of powers is suggested. Here we use eight powers {0, 0.1, 0.25, 0.5, 0.67, 1.0, 1.5, 2.0} per search radius. See Cook et al. (2013) for the functional forms of these correlation weightings. These transformations are monotonic, continuous, and cover the full range of weightings as a function of r and chosen p. When $p = 0$, $w\mathrm{TR} = u\mathrm{TR}$. A $p = 1.0$ indicates a linear weighting by the simple correlation; $p = 2.0$ indicates a weighting by the square of the correlation. Both have intuitively appealing interpretations with regard to relationships between variables, and simple correlation weighting ($p = 1.0$) has been used in previous climate reconstructions (e.g., Smerdon et al. 2015; Tierney et al. 2015). Principal components analysis (PCA) applied to each correlation-weighted covariance matrix thus produces a set of orthogonal projection coefficients (PCs) that are weighted differentially by the climate variable being reconstructed. Run this way, PCR produces an ensemble of eight reconstructions per search radius that can be compared and pooled into an ensemble mean reconstruction. This has been done for the drought atlases produced by Cook et al. (2015), Palmer et al. (2015), and Stahle et al. (2016). Correlation-weighted PCR is used in this way here as well.

Prior to weighting, autoregressive (AR) modeling was applied to the tree-ring chronologies and grid point precipitation data for each season using the ''random shock'' method of Meko (1981). AR modeling applied this way corrects for differences in persistence between tree rings and precipitation to produce less biased reconstructions of the latter. The AR modeled chronologies found within each search radius were then weighted by their correlations with seasonal precipitation as described above, and PCA was used to identify the main modes of covariance between the correlation-weighted chronologies. The time series of PC scores (or amplitudes) were then used as candidate predictors of seasonal precipitation at each grid point (Cook et al. 2015) and the final regression model is based on those predictors with regression t statistics > 1.0. For most of the fitted regression models, this was also equivalent to minimizing the bias-corrected Akaike information criterion (Hurvich and Tsai 1989), but the selected $t > 1.0$ model was sometimes more parsimonious. To extend the reconstructions back in time as the shorter predictor chronologies drop out (e.g., supplemental Fig. SM-2), PCR was repeated for nested subsets of increasing length (Cook et al. 2004). The variance of each nested subset was scaled to the variance of instrumental precipitation during the calibration period. If a candidate reconstruction nest was correlated below $r = 0.2$ with the first fully replicated nest (for their full common interval; typically $n > 150$, with $p < 0.01$), then that candidate was not used and the grid point reconstruction would end with the previous nest [the skill statistics for these nested subsets are provided online (http://drought.memphis.edu/NASPA)].

The 16 individual ensemble reconstructions for each season (using the eight 500- and eight 1000-km members) were averaged with a biweight robust mean to provide the initial gridded estimates of cool- and warm-season precipitation. A nine-point regression kernel based on the ''queen's case'' adjacency model used in spatial statistics was then applied to each grid point reconstruction to re-estimate and locally smooth the field of reconstructions. In the process, if any of the surrounding eight reconstructions was longer than the center gridpoint reconstruction, then the center reconstruction was extended or imputed back in time. On the basis of the queen's-case adjacency model and the way in which it locally imputes and provides smoothing to the field, we call this nine-point regression kernel procedure queen's-case imputation and smoothing (QCIS).

The QCIS procedure also reduces the number of erratic or inconsistent grid point estimates between adjacent grid points in a given year caused by stochastic variability in the fitted PPR models, and the imputation component more completely fills in spatial discontinuities in the final reconstruction fields. As such, QCIS can also be applied iteratively to previously QCIS-processed fields to increase the spatial smoothing and imputation. For the NASPA, three iterations of QCIS were used to complete the cool- and warm-season precipitation reconstructions, and the calibration and validation statistics reported here are based on this third iteration.

The reconstructions were evaluated on the basis of calibration (1928–78) and validation period (1901–27) statistics (Cook et al. 1999), including the calibration period coefficient of multiple determination (CRSQ) and the leave-one-out cross-validation reduction of error (CVRE), which is similar to Allen's prediction error sum of squares (Allen 1974). CVRE is a more conservative measure of fractional explained variance and can even go negative, thus making it useful as a regression diagnostics tool (Quan 1988). For the verification period, the Pearson correlation coefficient squared (VRSQ), the reduction of error (VRE), and the coefficient of efficiency (VCE) were computed. The CVRE is a less biased measure of the calibrated variance than the CRSQ and may provide the most realistic estimate of the seasonal precipitation skill in the reconstructions only because the instrumental precipitation data are quite limited in some regions of North America during the early-twentieth century. We note below some additional qualitative "validation" provided by the similarity between the large-scale teleconnection patterns in instrumental and reconstructed precipitation during the late-nineteenth and twentieth century.

Despite the selection of tree-ring predictors with discrete cool or warm-season precipitation signal, the correlation between reconstructed DJFMA and MJJ precipitation is still higher at most grid points than the interseasonal correlation observed with instrumental cool- and warm-season totals (online supplemental Fig. SM-4). Persistence-free estimates of reconstructed MJJ precipitation (MJJpf) were therefore calculated at each grid point using the residuals from the regression of reconstructed MJJ precipitation totals on DJFMA totals for the period from 1400 to 2016 when the seasonal reconstructions are adequately replicated over most of the continent (further described in the online supplemental material and Figs. SM-4 and SM-5). These residuals were then rescaled to units of MJJ precipitation (mm) by regression with the instrumental MJJ precipitation totals at each grid location during the calibration period 1928–78. The persistence-free MJJ totals were also used to calculate persistence-free records of SPI. The gridded MJJpf estimates of precipitation and SPI are restricted to the period from 1400 to 2016 and are used below with the DJFMA reconstructions for the temporal and spatial analysis of cool- and warm-season precipitation over the past 600 years.

4. Results

a. Discrete cool- and warm-season chronologies

A total of 439 tree-ring chronologies with a discrete correlation with DJFMA precipitation totals were selected for the reconstruction of "cool season" precipitation (Fig. 3a), and 547 chronologies discretely correlated with MJJ precipitation were selected for the reconstruction of "warm season" precipitation (Fig. 3b). The network of cool-season chronologies is extensive over western North America, but is limited over eastern Canada and the northcentral United States (Fig. 3a). The warm-season chronologies are more evenly distributed across the United States but are limited over eastern Canada and central Mexico (Fig. 3b). Naturally, these gaps in the spatial distribution of seasonal tree-ring chronologies tend to coincide with areas of low reconstruction skill (Figs. 4 and 5).

Total ring-width chronologies dominate the predictor network for both seasons (345 for the cool season and 342 for the warm season; Figs. 3a,b), but the discrete EW and LW chronologies were essential for the cool-season precipitation reconstructions in western Canada, the southeastern United States, and Mexico (Fig. 3a). For the warm-season reconstructions, most of the chronologies used south of 35°N were LW or LW*a* (Fig. 3b). Some of the total RW chronologies are discretely correlated with prior summer precipitation totals (*p*RW; Fig. 3b). These chronologies are located primarily in the northeast and northwestern part of the study area where favorable summer moisture levels can increase stored photosynthate and lead to improved radial growth during the following growing season (Aloni 1991; Watson and Luckman 2002).

The strength of the seasonal precipitation signal in the individual cool- and warm-season tree-ring chronologies is mapped based on the highest Spearman correlation at any point among the nine closest grid points to each chronology for the period 1928–78 (Figs. 3c,d; note that these correlation coefficients do not represent the full reconstruction skill possible with the point-by-point regression methods, as documented in Figs. 4 and 5). The Spearman correlations range from 0.26 to 0.90 (and from −0.26 to −0.58) for the cool season, with the highest correlations computed for California, Arizona, and the Sierra Madre Occidental of Mexico. The negative correlations in the Pacific Northwest are realistic in terms of bioclimatology and were computed for conifer chronologies inhibited by heavy winter snowpack. The warm-season correlations range from 0.26 to 0.73, but correlations above 0.50 are computed widely across the United States and Canada and contribute greatly to warm-season reconstruction skill (Fig. 3d).

b. Calibration and validation of the seasonal precipitation reconstructions

The calibration and validation statistics for the seasonal precipitation reconstructions are mapped for each grid point in Figs. 4 and 5. The discrete cool-season

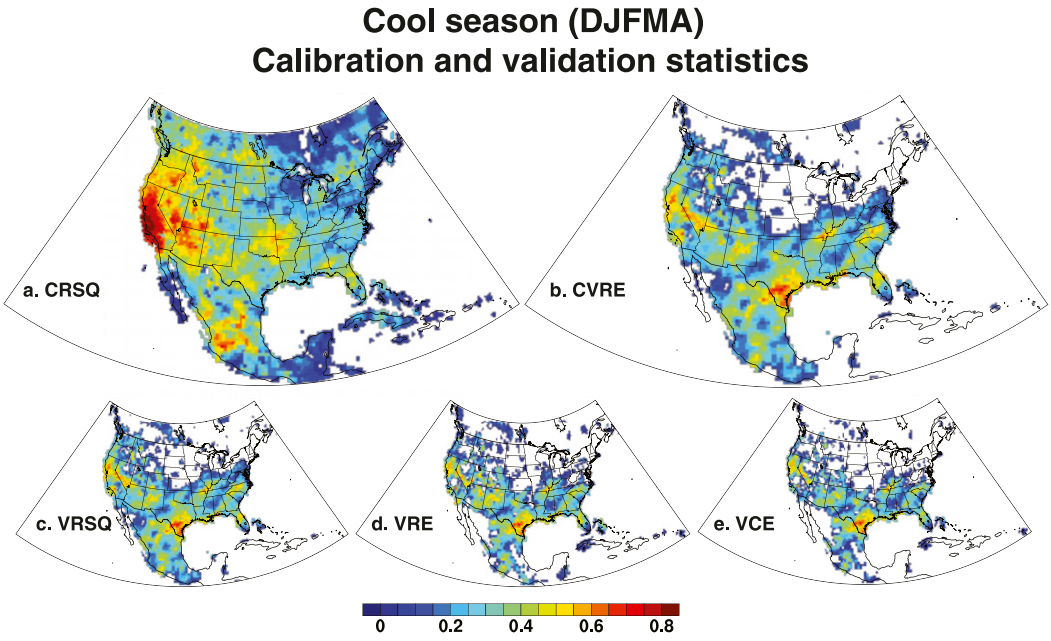

FIG. 4. The calibration and validation statistics computed for the tree-ring estimates of cool-season (DJFMA) precipitation totals are mapped for the 6812 grid points over North America. The calibration interval was 1928–78, and the validation interval was 1901–27 (calibration statistics: CRSQ = coefficient of multiple determination and CVRE = cross validation reduction of error; validation statistics: VRSQ = Pearson correlation coefficient squared, VRE = reduction of error, and VCE = coefficient of efficiency).

predictors capture over half of the variance in instrumental DJFMA precipitation totals for most of western North America extending from southwestern Canada across the western United States and into central Mexico (Fig. 4a). Over 40% of the cool-season precipitation variance is reconstructed for most of the south-central and southeastern United States (Fig. 4a). The coefficient of multiple determination (CRSQ) computed during the calibration interval 1928–78 ranges from 0.00 to 0.86 over the entire continent (i.e., all 6812 grid points). CRSQ is

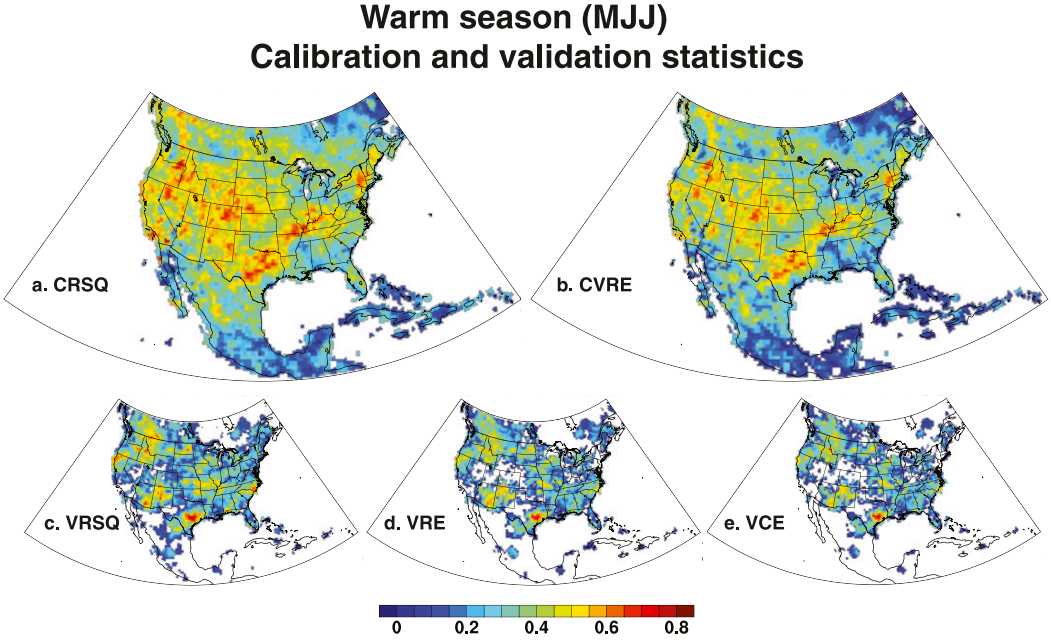

FIG. 5. As in Fig. 4, but for the tree-ring reconstructions of warm-season (MJJ) precipitation totals.

above 0.7 for many grid points in California, but is below 0.2 over much of eastern Canada, Baja California, the Yucatan Peninsula, and the Caribbean where few cool-season-sensitive tree-ring chronologies have been developed (Fig. 3a). The weakest calibrated region is in the northern Great Plains and Canada, as shown by the void in the CVRE map associated with negative CVREs (Fig. 4b). This is consistent with the low number of chronologies with a significant cool-season signal in those regions (Figs. 3a,c). However, even the stringent validation statistics computed during the independent interval from 1901 to 1927 indicate strong statistical validation of the cool-season precipitation reconstructions over most of subtropical North America extending from California eastward to the southeastern United States where early instrumental observations are abundant, including the VRSQ, the VRE, and the VCR (Figs. 4c–e).

The discrete warm-season chronologies reproduce over half of the instrumental MJJ precipitation variance for most of southern Canada, the United States, and portions of northcentral Mexico (Fig. 5a; the CRSQ statistic for the MJJ estimates ranges from 0.00 to 0.74 across all 6812 grid points). The MJJ precipitation reconstructions are well validated over most of this domain (Figs. 5b–e) with the exception of Ontario, the central Rocky Mountains, and northwestern Mexico (Figs. 5d,e). A comparison of the CVRE statistics based on the calibration interval 1928–78 (Fig. 5b) with the VRE and VCE computed on the validation period 1901–27 (Figs. 5d,e) indicates that there is useful skill in the tree-ring estimates and that the poor validation period results in these remote regions may again arise in part from limited instrumental precipitation observations during the early-twentieth century. The spatial distribution of precipitation stations included in the GPCC compilation is illustrated for two decadal episodes over the past 120 years (Fig. 2). Very few if any gauge records are available in the areas that exhibit weak validation period statistics for both the cool- and warm-season precipitation reconstructions during the first decade of the twentieth century, including portions of the northern Great Plains (Fig. 2a). Even during the 1970s decade of maximum station coverage, many poor performing areas still have the weakest instrumental station coverage (Fig. 2b). When the tree-ring calibration and validation statistics are considered in light of the availability of instrumental precipitation observation, the reconstructions may provide useful estimates of seasonal precipitation totals in some data poor areas where the early-twentieth-century validation tests fail (e.g., Sonora; Fig. 5 and supplemental Fig. SM-1). The seasonal reconstructions may also provide useful supplementary data to help to constrain early instrumental period reanalyses.

c. *Dynamical signals in instrumental and reconstructed seasonal precipitation totals*

The spatial correlations between the important modes of ocean–atmospheric variability and reconstructed precipitation over North America, and the degree to which the gridded seasonal reconstructions reproduce the teleconnections to cool- and warm-season precipitation observed in the instrumental data constitutes a stringent test of validity for the NASPA reconstructions. These comparisons are based on the 1928 to 1978 calibration interval in common to both the instrumental and reconstructed precipitation data. Because instrumental measurements of ENSO and other modes of circulation in some cases begin in the midnineteenth century, we also correlate these earliest circulation indices with the reconstructed seasonal precipitation totals during the nineteenth and early-twentieth century largely prior to the availability of gridded instrumental precipitation data for North America. These ''precalibration'' correlations are all based on the 1872–1927 period and provide further insight into the fidelity of the reconstructions and the stability of large-scale climate teleconnections to North America at the beginning of instrumental observations and prior to the heaviest anthropogenic forcing of regional to global climate. The modes of ocean–atmospheric circulation tend to be most energetic and teleconnections most intense during the cool season, but we describe important circulation influences on both cool- and warm precipitation using the instrumental and reconstructed totals.

1) COOL SEASON

The strongest circulation influence on cool or warm-season precipitation over North America is associated with ENSO. There are highly significant point-wise positive correlations ($p < 0.001$) between the November–February (NDJF) extended multivariate ENSO index (eMEI; Wolter and Timlin 2011) and cool-season precipitation totals over subtropical North America in both the instrumental and reconstructed data, particularly over northern Mexico and the southwestern United States (Figs. 6a,b). There is a significant negative correlation between the NDJF eMEI and cool-season precipitation over the Pacific Northwest, southern Canada, and the Ohio Valley (Figs. 6a,b). Instrumental and reconstructed cool-season precipitation totals are also correlated with indices of the Pacific/North American pattern (PNA; online supplemental Fig. SM-6) and the Pacific decadal oscillation (PDO; Fig. SM-7), but the

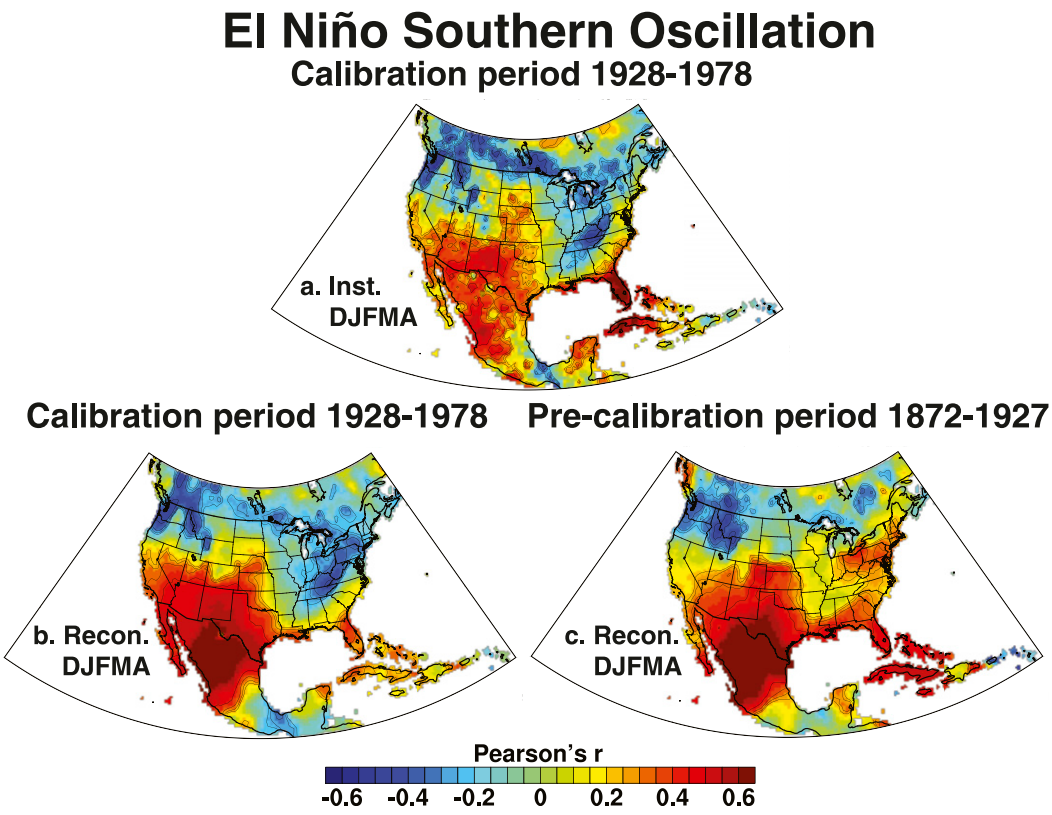

FIG. 6. The correlation between the November–February eMEI (Wolter and Timlin 2011) and gridded (a) instrumental and (b) reconstructed cool-season precipitation totals for the period 1928–78. (c) As in (b), but for the precalibration period from 1872 to 1927 using tree-ring-reconstructed cool-season totals and the instrumental eMEI. Four levels of significance are indicated by the contours (p = 0.10, 0.05, 0.01, and 0.001). Regions without reconstructed validation skill in the early-twentieth century are mapped in Fig. 4, but the similarity between instrumental and reconstructed patterns of ENSO correlation lends credibility to the reconstructions even in some areas without statistical validation from 1901 to 1927.

spatial patterns of correlation tend to be weaker and closely resemble the ENSO teleconnection. However, the PDO in particular may interact with other modes of ocean–atmospheric forcing to result in significant impact on cool-season precipitation over North America (e.g., Gershunov and Barnett 1998).

The reconstructions reproduce the spatial pattern of the ENSO teleconnection to instrumental precipitation with great fidelity, including the detailed geographical structure to the signal over the Pacific Northwest and southern Mexico. However, the area and magnitude of correlation over northern Mexico and the Southwest is stronger, and the correlation over Florida is weaker in the reconstructions than in the instrumental data (Figs. 6a–c). These differences are due in part to the nature of the PPR reconstruction method and the search radii that were used. The enhanced ENSO signal over the ''TexMex'' sector may also be due in part to the additional though weak October–November precipitation response in of some the predictor tree-ring chronologies from the region (not shown), correlation with seasonal temperature conditions in some tree-ring data, and the limited instrumental observations from Mexico before 1950 (e.g., Stahle et al. 2016).

The pattern and intensity of the ENSO signal in cool-season precipitation during the late-nineteenth and early-twentieth century (Fig. 6c) is very similar to the twentieth-century response (Figs. 6a,b), although the significant positive correlations weakened over California while they strengthened across the eastern United States. The negative ENSO correlation observed in the Ohio Valley during the period 1928–78 was not present in the reconstructions from 1872 to 1927 (Fig. 6c), as noted by Cole and Cook (1998) and Torbenson et al. (2019). These comparisons suggest that the ENSO signal to North America has been most stationary only over the TexMex and Pacific Northwest sectors during the past 146 years.

The North Atlantic Oscillation (NAO) is the sea level pressure gradient between the subpolar low and subtropical high over the North Atlantic Ocean that influences cool-season weather and climate in eastern North America and especially Europe (Hurrell et al. 2003). The NAO for DJFMA is significantly correlated with instrumental and reconstructed cool-season precipitation over the Ohio and Lower Mississippi Valleys, where DJFMA precipitation tends to be enhanced during the positive phase of the NAO (online supplemental Figs. SM-8a,b; https://crudata.uea.ac.uk/cru/data/nao/nao.dat). This enhanced cool-season precipitation response to the positive NAO is consistent with analyses of instrumental data and some model simulations (Durkee et al. 2008; Ning and Bradley 2016; Whan and Zwiers 2017). It is also consistent with analyses of instrumental and tree-ring-reconstructed Palmer drought indices (Fye et al. 2006). However, the NAO correlation with reconstructed DJFMA precipitation weakened over the central United States during the late-nineteenth and early-twentieth century (Fig. SM-8c). The reason for this nonstationarity is not clear, but the NAO teleconnection to instrumental and reconstructed DJFMA precipitation also weakened during the earliest period of instrumental GPCC precipitation observations from 1892 to 1927 (not shown).

The Arctic Oscillation (AO) is an annular mode of zonal circulation between 35° and 55°N (Ambaum et al. 2001). The NAO and PNA are related to the AO (Ambaum et al. 2001), and the correlation between indices of the NAO and AO for the winter to midspring season (DJFMA) is $r = 0.68$ ($p < 0.001$; 1928–78). Consequently, the AO is also positively correlated with instrumental and reconstructed cool-season precipitation totals over the Ohio Valley during the calibration period 1928–78 similar to the pattern of correlation with the NAO (not shown). However, the correlation between the AO and warm-season precipitation reverses sign from the cool season to the warm season when the May–June AO index becomes negatively correlated with MJJ and MJJpf precipitation over the central United States. This change in the response of precipitation to the AO may be broadly due to the poleward migration of the jet stream from the cool season to the warm season.

2) WARM SEASON

The AO index is computed as the leading PC of monthly mean Northern Hemisphere sea level pressure field (20°–90°N; Thompson and Wallace 2001). The AO tends to weaken in the warm season, but a significant negative correlation between the summer AO index and summer precipitation over the central United States has nevertheless been previously detected (Hu and Feng 2009). This negative AO signal is also detected in the instrumental and reconstructed MJJ or MJJpf precipitation totals and SPI extending from the Great Plains across the Ohio Valley and into the northeastern United States (Figs. 7a–c, online supplemental Figs. SM-9a,b). The strongest correlations with MJJ totals are computed with just the May–June AO index (Fig. 7 and Fig. SM-9), but the full warm-season (MJJ) AO index is also well correlated with gridded MJJ precipitation in the instrumental and reconstructed data (not shown).

The correlation between the May–June AO index during the 1872–1927 period is similar to the correlations for 1928–78 (Figs. 7a–c), indicating that the Arctic Oscillation has been an important factor in warm-season precipitation variability over North America for the past 150 years. The positive phase of the AO is associated with a northward shift of the jet stream and with subsidence, moisture divergence, and reduced warm-season rainfall over the central United States (Hu and Feng 2009) where the instrumental and reconstructed data are negatively correlated with the AO. The AO is also positively correlated with MJJ precipitation totals over southwestern North America (Fig. 7) and may therefore play a role in promoting the North American monsoon. The NAO index averaged for May–June is also significantly and negatively correlated with instrumental and reconstructed MJJ precipitation over the central United States from 1892 to 1927 (similar to the AO; not shown). This negative NAO correlation weakens from 1928 to 1978, but still contrasts with the positive DJFMA NAO teleconnection to cool-season precipitation over this region (supplemental Fig. SM-8).

The influence of the Atlantic multidecadal oscillation (AMO), detrended area average SSTs in the Atlantic north of 0° (Enfield et al. 2001), has also been detected in warm-season precipitation totals, primarily over northern Mexico and the Southwest (McCabe et al. 2004; Seager et al. 2007). The annual average AMO (August–July: http://www.esrl.noaa.gov/psd/data/timeseries/AMO/) is negatively correlated with instrumental and reconstructed MJJ and MJJpf precipitation over portions of northern Mexico and the southern United States for the calibration period (online supplemental Figs. SM-10a,b,d), but only over the Southwest during the precalibration interval (Figs. SM-10c,e). The AMO is not strongly correlated with cool-season precipitation over North America (not shown). Because of the strong persistence in the AMO index, composite analyses of the precipitation reconstructions were also computed for the phases of the AMO. Modestly dry conditions prevailed over southwestern North America during the positive phases of the AMO (i.e., 1857–1901

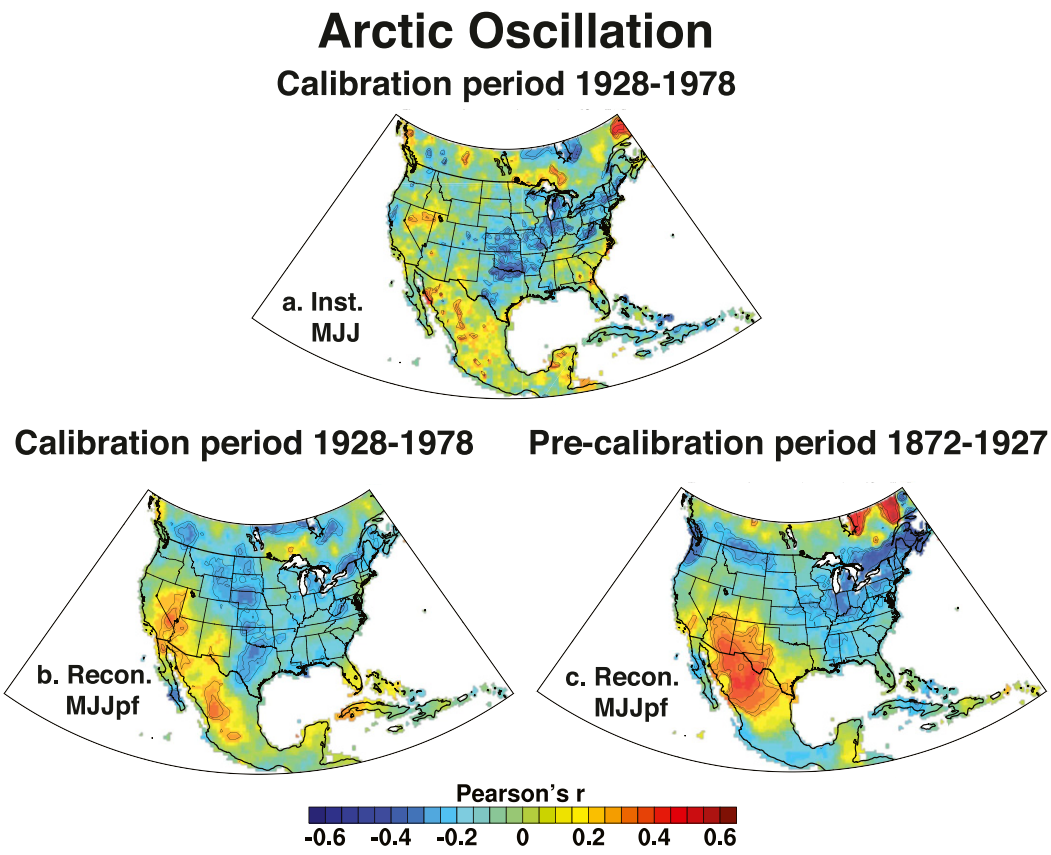

FIG. 7. As in Fig. 6, but for the Arctic Oscillation index averaged for May and June, correlated with (a) instrumental MJJ and (b),(c) reconstructed MJJpf precipitation totals.

and 1931–63) and slightly wet conditions during negative phases (1902–30 and 1964–95; not shown), consistent with the correlation analyses in Fig. SM-10.

d. Cool- and warm-season precipitation variability over North America

For a time series perspective on the seasonal precipitation reconstructions, the cool- and warm-season precipitation estimates are plotted from 1400 to 2016 for nine 10° × 10° regions of North America in online supplemental Figs. SM-11 and SM-12, including the south-central United States (Fig. 8 and Figs. SM-11m,n and SM-12m,n) where the cool- and warm-season reconstructions are well calibrated and validated [Figs. 4 and 5; and where the persistence-free warm-season estimates are also correlated with instrumental MJJ precipitation (supplemental Figs. SM-5a,b)]. The reconstructions for the south-central United States indicate more frequent and severe cool- and warm-season drought during the fifteenth century (Figs. 8a,b), although reduced sample size and scaling of the nested reconstructions may impact the intensity of these ancient droughts and deserve further study. The regional reconstructions indicate large seasonal differences in the severity and persistence of certain moisture regimes, including the pluvial in the early nineteenth century that was one of the wettest warm-season decades of the past 600 years, but was near normal during the cool season (1803–12; Figs. 8a,b). The warm-season reconstructions also exhibit significant linear trends in MJJpf precipitation totals from 1400 to 2016 ($p = 0.01$; Fig. 8b). Long-term trends are less pronounced in the cool-season reconstruction for the south-central United States, but the twentieth century is here estimated to have been the wettest 100-yr cool-season episode since 1400 (Fig. 8a).

The midnineteenth-century drought was one of the most severe preindustrial droughts of the past 500 years based on the long-term soil moisture balance reconstructions in the NADA (Fye et al. 2003; Herweijer et al. 2006). The NASPA seasonal precipitation reconstructions indicate that dry conditions were widespread over North America during both the cool and warm seasons from 1855 to 1864 (Fig. 9). However, the center of intense drought during the midnineteenth century appears to have shifted from the Southern Plains in the cool season into the Northern Plains and Northern Rockies

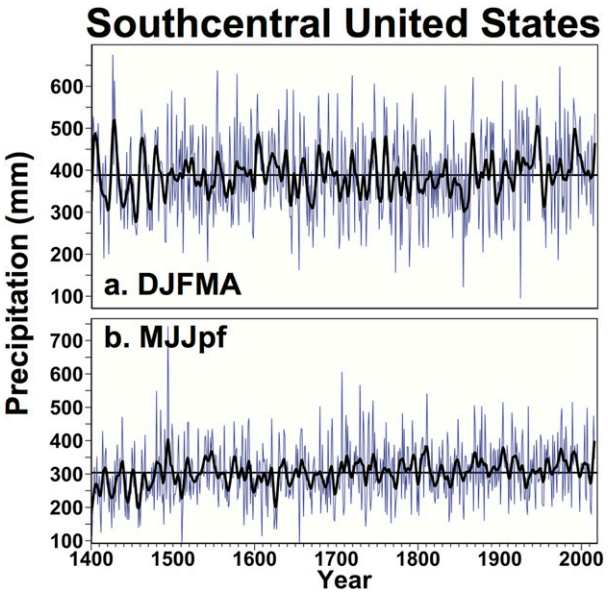

FIG. 8. Tree-ring-reconstructed (a) cool- (DJFMA) and (b) warm-season (MJJpf) precipitation totals, plotted from 1400 to 2016 for the south-central United States (29°–39°N, 90°–100°W). Annual values are illustrated in blue. The black curve is a fitted spline emphasizing decadal variability. Regional average reconstructions are plotted for eight other subregions of North America in supplemental Fig. SM-12.

during the warm season (Figs. 9a,b). Near-normal to above-average MJJpf precipitation is estimated for the lower Mississippi and Ohio Valleys in strong contrast to the intense decadal drought reconstructed for the cool season during the midnineteenth century (Figs. 9a,b).

Out-of-phase seasonal moisture conditions lasting 10 years or longer are not common in the reconstructions or in the instrumental record, but dryness prevailed in the warm season over the eastern United States during the mideighteenth century when cool-season precipitation was near normal (Figs. 9c,d). The intense pluvial over western North America during the final decade of the pre-Columbian era (1483–92) extended from Mexico to the northern Great Plains during the cool season, but dry conditions developed during the warm season over much of this same sector of western North America in one of the largest decade-scale reversals of cool- to warm-season precipitation in the new reconstructions (Figs. 9e,f).

The sixteenth-century megadrought was the most severe and sustained drought of the past 500 years based on the gridded PDSI reconstructions in the NADA (Stahle et al. 2000; Cook et al. 2004). The sixteenth-century megadrought impacted most of North America during the mid- to late 1500s (Meko et al. 1995; Stahle et al. 2007) and has been associated with intense and prolonged cool conditions in the equatorial Pacific (Cook et al. 2018). The new NASPA reconstructions indicate that the sixteenth-century megadrought may actually have been two or even three separate droughts, possibly involving different climate dynamics. The start and end dates of the megadrought varied spatially during the late-sixteenth century (Stahle et al. 2007; Cook et al. 2018), but from 1568 to 1591 cool-season drought prevailed over the Southwest, northern Mexico, and the eastern United States along with wetness over southern Mexico (Fig. 10a). Warm-season drought prevailed over the midwestern United States and persisted from winter to summer over Arizona and Sonora (Fig. 10b). The seasonal and spatial patterns of these late-sixteenth-century precipitation regimes bear some resemblance to the continent-wide teleconnection anomalies associated with La Niña events during the cool season (note Figs. 6a,b and 10a), the Arctic Oscillation during the warm season over the central United States (Figs. 7a–c and 10b), and possibly the Atlantic multidecadal oscillation for the warm season over the Southwest (Figs. 10b,c and supplemental Fig. SM-10).

By design, the long-term soil moisture reconstructions developed for the NADA (Cook et al. 1999, 2010a) integrate the three regional and seasonal droughts of the late-sixteenth century into a prolonged episode of coast-to-coast dryness (Fig. 10c; Cook et al. 2018). This integration may obscure part of the explanation for this multidecadal episode of severe and sustained drought, however. The NASPA reconstructions in Fig. 10 suggest that the continent-wide megadrought of the late-sixteenth century may have developed from the convergence of cool-season drought over subtropical North America involving ENSO with warm-season droughts over the central and southwestern United States involving the AO and AMO. What is not clear, however, is how these three modes of atmospheric circulation, which are known to influence North American regional precipitation totals on interannual time scales, may have each persisted or recurred with sufficient frequency to have influenced the 24-yr moisture regimes reconstructed for the late-sixteenth century.

e. Secular trend in seasonal precipitation over North America

The positive trend in reconstructed warm-season precipitation totals over the south-central United States (Fig. 8b) is part of a significant wetness trend reconstructed for the cool and warm seasons over much of eastern North America. However, this large-scale wetness trend appears to have been longer and stronger in the warm season. The precipitation reconstructions at each grid point were tested for linear trend using two time intervals that appear to include some of the strongest and most widespread changes in reconstructed

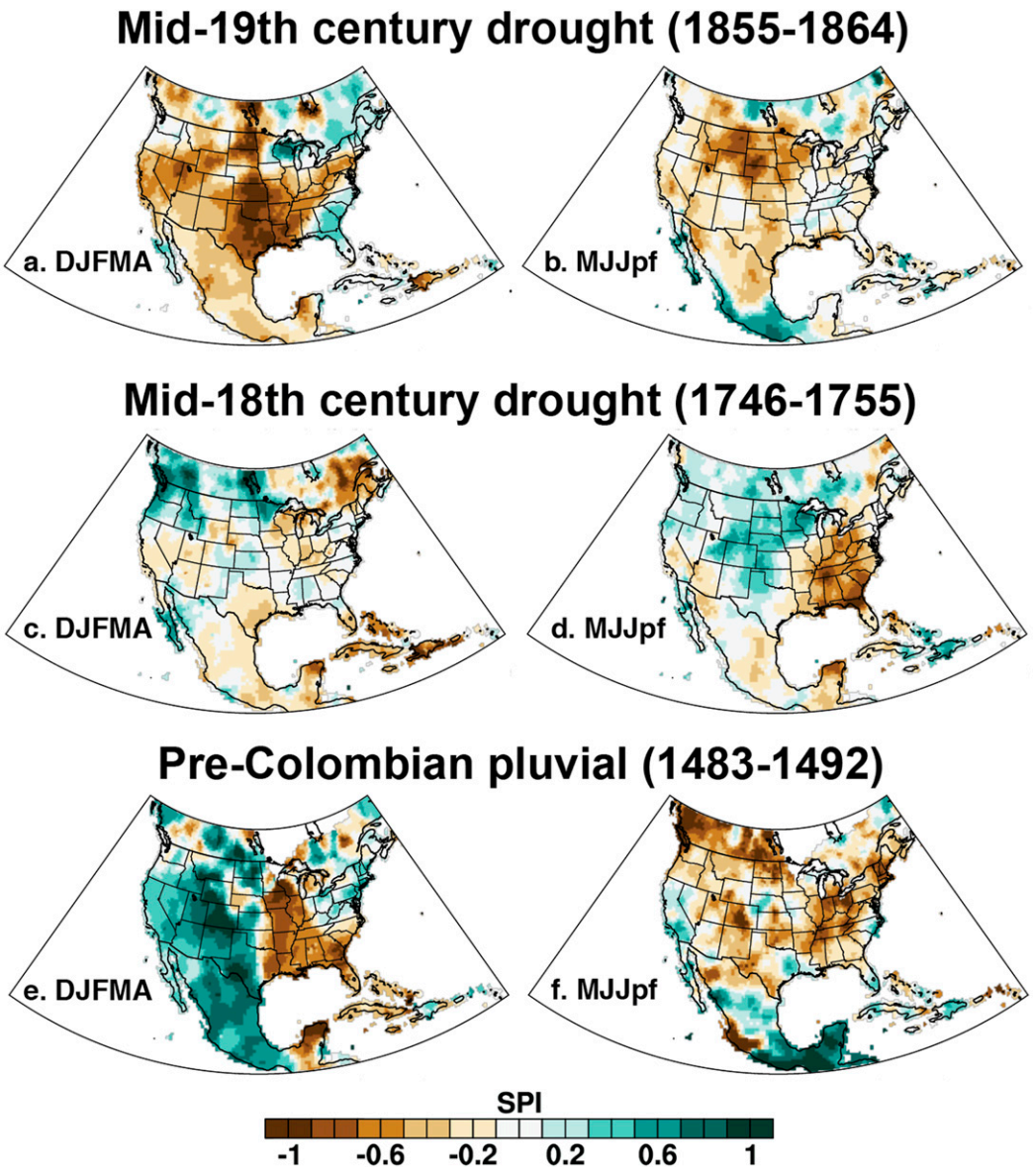

FIG. 9. Tree-ring-reconstructed (a) cool-season (a) and (b) persistence-free warm-season SPI during the midnineteenth-century drought are averaged and mapped for the decade from 1855 to 1864. The most intense 10 years of the (c),(d) mideighteenth-century drought (1746–55) and the (e),(f) pre-Columbian pluvial (1483–92) are also mapped using SPI for the seasonal precipitation reconstructions.

precipitation for each season. The robust Theil–Sen slope statistic is mapped for each gridded cool-season reconstruction for the interval 1800–2016 (Fig. 11a) and for the persistence-free warm-season reconstructions from 1500 to 2016 (Fig. 11b). Significant long term and positive trend is identified over eastern North America during the cool and especially the warm seasons. Groisman et al. (2004) also note stronger warm-season precipitation trend in instrumental observations for the eastern United States from 1900 to 2002. Hoerling et al. (2016) identify positive trend in heavy warm-season precipitation events over the Midwest and Northeast (1979–2013). Data from NOAA's National Centers for Environmental Information indicate significant positive trend ($p < 0.05$) for summer precipitation over the Midwest but no significant trend over the 48 contiguous United States in winter from 1895 to 2018 (http://www.ncdc.noaa.gov/temp-and-precip/us-trends/).

A long-term trend in wetness over eastern North America has been previously identified by paleoclimate and modern climate research, including trend at millennial (Shuman and Marsicek 2016), centennial

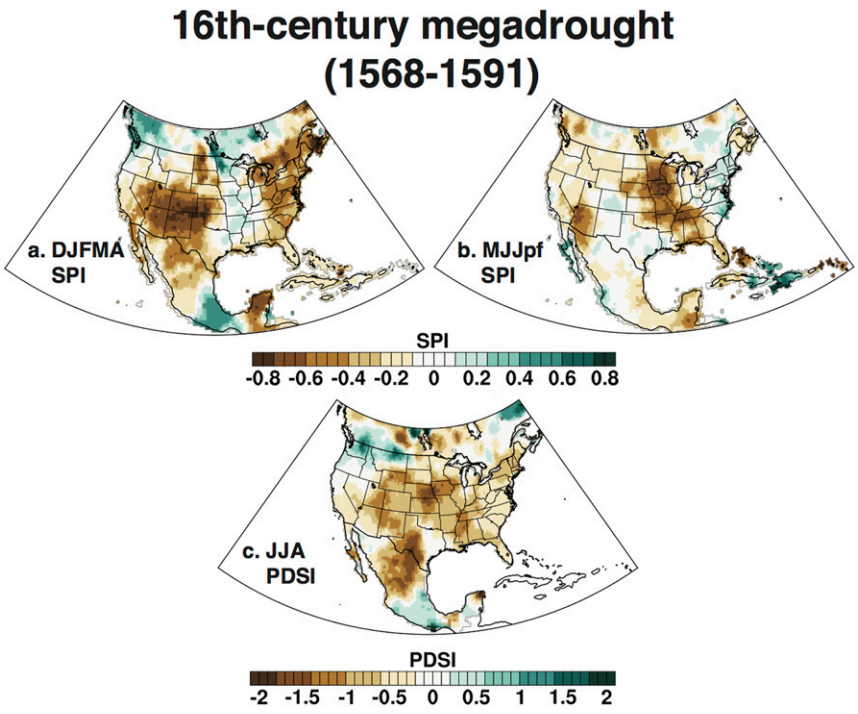

FIG. 10. (a),(b) As in Fig. 9, but for tree-ring-reconstructed SPI for the 24-yr interval from 1568 to 1591 during the sixteenth-century megadrought. (c) The tree-ring reconstructions of summer PDSI for 1568–91 are also mapped from the NADA (Cook et al. 2010a).

(Pederson et al. 2013; Newby et al. 2014), and decadal time scales (Groisman et al. 2004, 2005; Seager et al. 2012; Bishop et al. 2019). The millennial-scale trends have been related to large-scale cooling and increased effective moisture over the Northern Hemisphere since the mid-Holocene (Shuman and Marsicek 2016), but the more recent wetness trends are not well understood (Pederson et al. 2013). Anthropogenic warming and wetting of the atmosphere may have contributed to the positive trend in total precipitation over the eastern United States in recent decades, and to the increase in very heavy precipitation events in the midlatitudes (Groisman et al. 2005). However, other analyses suggest that the trend in precipitation, extreme precipitation, or water vapor in the East may have arisen only from internal atmospheric variability (e.g., Seager et al. 2012; Kunkle et al. 2013; Hoerling et al. 2016). Because the trends in reconstructed seasonal totals begin before the onset of the industrial revolution and heavy anthropogenic climate forcing, natural variability may be implicated in at least the initiation of these long-term precipitation changes in eastern North America.

These tests of trend in the precipitation reconstructions are sensitive to the time interval of analysis, and the area of significant negative trend in reconstructed cool-season precipitation over the Pacific Northwest is more widespread when based on the 300-yr period from 1700 to 2016 (not shown; see also Pederson et al. 2011). The reconstructed precipitation trends are also modest in terms of the absolute change in total precipitation. The warm-season trend in MJJpf precipitation from 1500 to 2016 for the south-central United States (Fig. 8b) is $0.063\,\mathrm{mm\,yr^{-1}}$ ($p < 0.01$), or approximately 10.8% of the long-term warm-season mean from 1400 to 2016. The shorter trend in cool-season precipitation for the south-central United States from 1800 to 2016 (Fig. 8a) was $0.267\,\mathrm{mm\,yr^{-1}}$ ($p < 0.05$), or some 15.0% of the reconstructed cool-season mean from 1400 to 2016.

The reconstructions of seasonal precipitation are inevitably based on many fewer tree-ring chronologies during the earliest years of record in the nested estimates. This means that there is a greater likelihood of extrapolating regional tree-ring estimated precipitation information over a larger spatial domain for the earliest years in the NASPA. But the reconstructions nonetheless provide important and spatially specific insight into centennial scale variability in seasonal precipitation totals. The need to better understand these long-term precipitation changes, both from the perspective of climate dynamics and water resources planning, justifies a concerted effort to expand the collection of millennium-long tree-ring chronologies

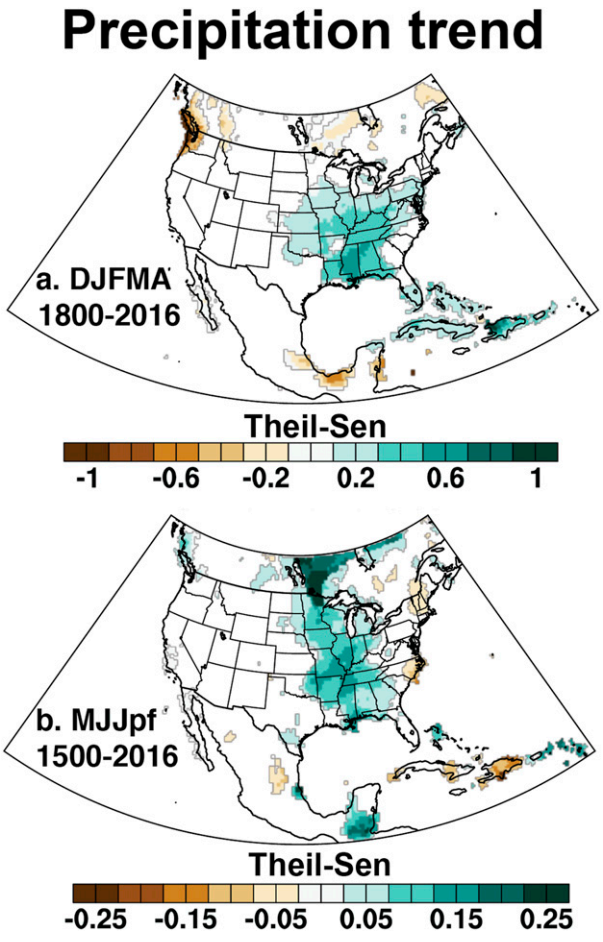

FIG. 11. On the basis of the Theil–Sen slope estimate, significant positive trend has been detected over the eastern United States (a) in reconstructed cool-season precipitation since 1800 and (b) in reconstructed warm-season precipitation since 1500.

sensitive to cool- or warm-season moisture, particularly over eastern North America.

5. Discussion and conclusions

The new tree-ring reconstructions of cool-, warm-, and persistence-free warm-season precipitation are based on a subset of North American tree-ring chronologies with discrete seasonal moisture signals. The reconstructions calibrate at least 40% of the variance for both December–April (cool season) and May–July (warm season) precipitation totals over a large portion of North America for up to 2000 years. The areas of lowest calibration and validation skill in both the cool- and warm-season reconstructions are located where few seasonal tree-ring chronologies or few instrumental observations are available. Development of additional long tree-ring chronologies with discrete seasonal precipitation signals is feasible and would lead to improved cool- and warm-season moisture reconstructions for North America.

The new reconstructions represent the first spatially explicit estimates of both cool- and warm-season precipitation amounts over much of the North American continent and are most strongly replicated with seasonally discrete tree-ring chronologies during the past 600 years. The reconstructions for the cool and warm seasons extend as far back as 2000 years where discrete seasonal predictors are available, but the persistence-free warm-season reconstructions are confined to the period 1400–2016. The reconstructions estimate strong, widespread, and seasonally persistent drought and wetness regimes, as well as other episodes of cool-to-warm-season precipitation reversals that may signify unusual configurations of ocean–atmospheric circulation. In both seasons, tree-ring-reconstructed precipitation over most of North America recorded more severe and sustained decadal droughts than were witnessed during the modern instrumental era, helping to document the range of persistent and widespread dryness that was possible under natural conditions prior to heavy anthropogenic forcing of regional and global climate.

The seasonal precipitation reconstructions are significantly correlated with indices of ENSO, the PDO, PNA, NAO, and the AO in winter, and with the AO and AMO during summer. The spatial correlations faithfully reproduce the teleconnection patterns present in the instrumental precipitation data and provide strong dynamical justification for the extraction of discrete seasonal climate information from the network of North American tree-ring chronologies. In fact, the sign of significant seasonal precipitation correlations with the AO reverses from the cool to warm season over the central United States as the jet stream and mean storm track shift poleward with the onset of summer. This change in the sign of AO forcing of seasonal precipitation is also detected in the long-term soil moisture balance reconstructions available in the NADA, but the magnitude and area of significant correlations with seasonal AO indices (i.e., DJFMA and MJ) are much lower in the instrumental and reconstructed JJA PDSI in the NADA.

The cool-season reconstructions indicate that the ENSO influence on DJFMA precipitation was as strong during the late-nineteenth and early-twentieth century as it was during the midtwentieth century, especially over northern Mexico where the teleconnection is arguably the strongest and most stable over time (Stahle et al. 2016; Torbenson et al. 2019). The Arctic Oscillation has the strongest correlation with instrumental and reconstructed warm-season precipitation in both the calibration period (1928–78) and with the reconstructed MJJ and MJJpf

totals during the late nineteenth and early twentieth century. Warm-season precipitation is suppressed over most of the continent during the positive phase of the AO, but it is enhanced over northern Mexico and the Southwest, especially in the reconstructed warm-season totals. The consistency of the ocean–atmospheric teleconnections to seasonal precipitation in both the instrumental and reconstructed totals provides important validation of the tree-ring reconstructions from the perspective of the internal climate dynamics that drive moisture variability across North America. These teleconnection results, coupled with the calibration and validation statistics, also indicate that the tree-ring reconstructions of seasonal precipitation may constitute the best seasonal precipitation estimates currently available for certain remote areas of Canada, the western United States, and Mexico during the early-twentieth century when station observations were limited or nonexistent.

The seasonal reconstructions indicate significant positive trend in cool- and warm-season precipitation that impacted most of the eastern United States. Enhanced precipitation amounts have been documented for eastern North America on an annual basis with other paleoclimate proxies (Pederson et al. 2013). The wetness trend in tree-ring-reconstructed warm-season precipitation began at least 500 years ago, and some 200 years ago for cool-season precipitation, and both may have been enhanced in recent decades by anthropogenic activity. The dynamics responsible for these moisture trends may involve a combination of factors related to anthropogenic warming (Groisman et al. 2005), but the reconstructions indicate that cool- and warm-season precipitation trends began well before the industrial revolution and may also involve internal climate variability. The seasonal and spatial differences in reconstructed precipitation trend might provide insight into the underlying factors responsible for increasing precipitation over eastern North America.

The sixteenth-century megadrought was the most severe, sustained, and continent-wide drought of the past 500 years based on the tree-ring reconstructions of PDSI provided by the North American Drought Atlas (Cook et al. 2010a), but the North American Seasonal Precipitation Atlas indicates that it may have been the combined result of three spatially distinct seasonal droughts. The seasonal moisture anomalies associated with these three co-occurring late-sixteenth-century droughts resemble the teleconnection patterns associated with ENSO, the AO, and the AMO in the instrumental and reconstructed precipitation data during the nineteenth and twentieth centuries. If these modes of ocean–atmospheric forcing of North American precipitation were active in the late-sixteenth century, then they may have contributed to the megadrought. Many examples of seasonal differences in the spatial pattern of precipitation can be found in the NASPA at interannual, decadal, and multidecadal time scales, and provide a rich source of precipitation variability that should be useful for investigations of North American climate dynamics and change during the late Holocene.

Acknowledgments. Support is from NSF Grants GEO/ATM-0753399, AGS-1266014, AGS-1266015, AGS-1301587, AGS-1502224, AGS-1702894, and EF-1241930. We thank Rodolfo Acuna Soto, Chris Baisan, Dan Bishop, Jordan Burns, Julian Cerano Paredes, Malcolm Cleaveland, Jeff Dean, Falko Fye, Paul Krusic, Mark Losleban, Martin Munro, Richard Seager, Jason Smerdon, Scott St. George, Paul Szejner, Matt Therrell, and Gene Wahl for assistance and advice, and we thank the many contributors to the International Tree-Ring Data Bank, particularly John King, Peter Brown, Jesse Edmondson, Lisa Graumlich, Richard Guyette, D. Rubino, Bill Callahan, Brian Luckman, Brendan Buckley, Mike Stambaugh, Tom Swetnam, Troy Knight, and Tony Caprio. The editor and three peer reviewers provided helpful suggestions that have improved this article. Any use of trade, firm, or product names is for descriptive purposes only and does not imply endorsement by the U.S. government. This is Lamont-Doherty Earth Observatory contribution number 8380.

Data availability statement: The instrumental and tree-ring-reconstructed cool- and warm-season precipitation data can be accessed online (http://drought.memphis.edu/NASPA/), where it is possible to create maps of instrumental or reconstructed DJFMA, MJJ, and MJJpf precipitation totals or standardized precipitation indices, plot time series for single points or user-selected regional averages, create correlation maps, access the calibration and validation statistics for all nested reconstructions, and perform many other analyses. The tree-ring data, both raw ring-width measurement series and the derived chronologies, the instrumental cool- and warm-season gridded GPCC precipitation data, and the gridded seasonal precipitation reconstructions are also all available online at ITRDB at NOAA Paleo (https://www.ncdc.noaa.gov/data-access/paleoclimatology-data/datasets/tree-ring).

REFERENCES

Allen, D. M., 1974: The relationship between variable selection and data augmentation and a method for prediction. *Technometrics*, **16**, 125–127, https://doi.org/10.1080/00401706.1974.10489157.

Aloni, R., 1991: Wood formation in deciduous hardwood trees. *Physiology of Trees*, A. S. Raghavendera, Ed., John Wiley and Sons, 175–197.

Ambaum, M. H. P., B. J. Hoskins, and D. B. Stephenson, 2001: Arctic Oscillation or North Atlantic Oscillation? *J. Climate*, **14**, 3495–3507, https://doi.org/10.1175/1520-0442(2001)014<3495:AOONAO>2.0.CO;2.

Baek, S. H., J. E. Smerdon, S. Coats, A. P. Williams, B. I. Cook, E. R. Cook, and R. Seager, 2017: Precipitation, temperature, and teleconnection signals across the combined North American, monsoon Asia, and Old World Drought Atlases. *J. Climate*, **30**, 7141–7155, https://doi.org/10.1175/JCLI-D-16-0766.1.

Becker, A., P. Finger, A. Meyer-Christoffer, B. Rudolf, K. Schamm, U. Schneider, and M. Ziese, 2013: A description of the global land-surface precipitation data products of the Global Precipitation Climatology Centre with sample applications including centennial (trend) analysis from 1901–present. *Earth Syst. Sci. Data*, **5**, 71–99, https://doi.org/10.5194/essd-5-71-2013.

Benson, L. V., T. R. Pauketat, and E. R. Cook, 2009: Cahokia's boom and bust in the context of climate change. *Amer. Antiq.*, **74**, 467–483, https://doi.org/10.1017/S000273160004871X.

Bishop, D., and Coauthors, 2019: Investigating the causes of increased twentieth-century fall precipitation over the southeastern United States. *J. Climate*, **32**, 575–590, https://doi.org/10.1175/JCLI-D-18-0244.1.

Burns, J. N., R. Acuna-Soto, and D. W. Stahle, 2014: Drought and epidemic typhus, central Mexico, 1655-1918. *Emerg. Infect. Dis.*, **20**, 442–447, https://doi.org/10.3201/eid2003.131366.

Cleaveland, M. K., 1986: Climatic response of densitometric properties in semiarid site tree rings. *Tree-Ring Bull.*, **46**, 13–29.

Coats, S., J. E. Smerdon, B. I. Cook, R. Seager, E. R. Cook, and K. J. Anchukaitis, 2016: Internal ocean-atmosphere variability drives megadroughts in western North America. *Geophys. Res. Lett.*, **43**, 9886–9894, https://doi.org/10.1002/2016GL070105.

Cole, J. E., and E. R. Cook, 1998: The changing relationship between ENSO variability and moisture balance in the continental United States. *Geophys. Res. Lett.*, **25**, 4529–4532, https://doi.org/10.1029/1998GL900145.

Cook, B. I., J. Smerdon, R. Seager, and S. Coats, 2014: Global warming and 21st century drying. *Climate Dyn.*, **43**, 2607–2627, https://doi.org/10.1007/s00382-014-2075-y.

——, A. P. Williams, J. E. Smerdon, J. G. Palmer, E. R. Cook, D. W. Stahle, and S. Coats, 2018: Cold tropical Pacific sea surface temperatures during the late sixteenth-century North American megadrought. *J. Geophys. Res. Atmos.*, **123**, 11 307–11 320, https://doi.org/10.1029/2018JD029323.

Cook, E. R., and G. C. Jacoby, 1977: Tree-ring-drought relationships in the Hudson Valley, New York. *Science*, **198**, 399–401, https://doi.org/10.1126/science.198.4315.399.

——, and K. Peters, 1997: Calculating unbiased tree-ring indices for the study of climatic and environmental change. *Holocene*, **7**, 361–370, https://doi.org/10.1177/095968369700700314.

——, D. M. Meko, D. W. Stahle, and M. K. Cleaveland, 1999: Drought reconstructions for the continental United States. *J. Climate*, **12**, 1145–1162, https://doi.org/10.1175/1520-0442(1999)012<1145:DRFTCU>2.0.CO;2.

——, C. Woodhouse, C. M. Eakin, D. M. Meko, and D. W. Stahle, 2004: Long-term aridity changes in the western United States. *Science*, **306**, 1015–1018, https://doi.org/10.1126/science.1102586.

——, R. Seager, M. A. Cane, and D. W. Stahle, 2007: North American drought: Reconstructions, causes, and consequences. *Earth-Sci. Rev.*, **81**, 93–134, https://doi.org/10.1016/j.earscirev.2006.12.002.

——, ——, R. R. Heim Jr., R. S. Vose, C. Herweijer, and C. Woodhouse, 2010a: Megadroughts in North America: Placing IPCC projections of hydroclimatic change in a long-term palaeoclimate context. *J. Quat. Sci.*, **25**, 48–61, https://doi.org/10.1002/jqs.1303.

——, K. J. Anchukaitis, B. M. Buckley, R. D'Arrigo, G. C. Jacoby, and W. E. Wright, 2010b: Asian monsoon failure and megadrought during the last millennium. *Science*, **328**, 486–489, https://doi.org/10.1126/science.1185188.

——, P. J. Krusic, K. J. Anchukaitis, B. M. Buckley, T. Nakatsuka, M. Sano, and PAGES Asia2k Members, 2013: Tree-ring reconstructed summer temperature anomalies for temperate East Asia since 800 C.E. *Climate Dyn.*, **41**, 2957–2972, https://doi.org/10.1007/s00382-012-1611-x.

——, ——, and T. Melvin, 2014: Program RCSigFree. Tree-Ring Laboratory, Lamont Doherty Earth Observatory of Columbia University, https://www.ldeo.columbia.edu/tree-ring-laboratory/resources/software.

——, and Coauthors, 2015: Old world megadroughts and pluvials during the Common Era. *Sci. Adv.*, **1**, e1500561, https://doi.org/10.1126/sciadv.1500561.

Durkee, J. D., J. D. Frye, C. M. Fuhrmann, M. C. Lacke, H. G. Jeong, and T. L. Mote, 2008: Effects of the North Atlantic Oscillation on precipitation-type frequency and distribution in the eastern United States. *Theor. Appl. Climatol.*, **94**, 51–65, https://doi.org/10.1007/s00704-007-0345-x.

Edwards, D. C., and T. B. McKee, 1997: Characteristics of 20th century drought in the United States at multiple time scales. Climatology Rep. 97-2, 155 pp., http://hdl.handle.net/10217/170176.

Elliott, K. J., C. F. Miniat, N. Pederson, and S. H. Laseter, 2015: Forest tree growth response to hydroclimatic variability in the southern Appalachians. *Global Change Biol.*, **21**, 4627–4641, https://doi.org/10.1111/gcb.13045.

Enfield, D. B., A. M. Mestas-Nunez, and P. J. Trimble, 2001: The Atlantic Multidecadal Oscillation and its relation to rainfall and river flows in the continental U.S. *Geophys. Res. Lett.*, **28**, 2077–2080, https://doi.org/10.1029/2000GL012745.

Fritts, H. C., 1966: Growth-rings of trees: Their correlation with climate. *Science*, **154**, 973–979, https://doi.org/10.1126/science.154.3752.973.

——, 1976: *Tree Rings and Climate*. Academic Press, 567 pp.

——, J. E. Mosiman, and C. P. Bottorff, 1969: A revised computer program for standardizing tree-ring series. *Tree-Ring Bull.*, **29**, 15–20.

Fye, F. K., D. W. Stahle, and E. R. Cook, 2003: Paleoclimatic analogs to twentieth-century moisture regimes across the United States. *Bull. Amer. Meteor. Soc.*, **84**, 901–910, https://doi.org/10.1175/BAMS-84-7-901.

——, ——, ——, and M. K. Cleaveland, 2006: NAO influence on subdecadal moisture variability over central North America. *Geophys. Res. Lett.*, **33**, L15707, https://doi.org/10.1029/2006GL026656.

Gershunov, A., and T. P. Barnett, 1998: Interdecadal modulation of ENSO teleconnections. *Bull. Amer. Meteor. Soc.*, **79**, 2715–2726, https://doi.org/10.1175/1520-0477(1998)079<2715:IMOET>2.0.CO;2.

Griffin, D., and Coauthors, 2013: North American monsoon precipitation reconstructed from tree-ring latewood. *Geophys. Res. Lett.*, **40**, 954–958, https://doi.org/10.1002/grl.50184.

Grissino-Mayer, H. D., and H. C. Fritts, 1997: The International Tree-Ring Data Bank: An enhanced global database serving the global scientific community. *Holocene*, **7**, 235–238, https://doi.org/10.1177/095968369700700212.

Groisman, P. Ya., R. W. Knight, T. R. Karl, D. R. Easterling, B. Sun, and J. H. Lawrimore, 2004: Contemporary changes of the hydrological cycle over the contiguous United States: Trends derived from in situ observations. *J. Hydrometeor.*, **5**, 64–85, https://doi.org/10.1175/1525-7541(2004)005<0064:CCOTHC>2.0.CO;2.

——, ——, D. R. Easterling, T. R. Karl, G. C. Hegerl, and V. N. Razuvaev, 2005: Trends in intense precipitation in the climate record. *J. Climate*, **18**, 1326–1350, https://doi.org/10.1175/JCLI3339.1.

Guttman, N. B., 1999: Accepting the standardized precipitation index: A calculation algorithm. *J. Amer. Water Resour. Assoc.*, **35**, 311–322, https://doi.org/10.1111/j.1752-1688.1999.tb03592.x.

——, J. R. M. Hosking, and J. R. Wallis, 1993: Regional precipitation quantile values for the continental United States computed from L-moments. *J. Climate*, **6**, 2326–2340, https://doi.org/10.1175/1520-0442(1993)006<2326:RPQVFT>2.0.CO;2.

Harris, I., P. D. Jones, T. J. Osborn, and D. H. Lister, 2014: Updated high-resolution grids of monthly climatic observations—The CRU TS3.10 dataset. *Int. J. Climatol.*, **34**, 623–642, https://doi.org/10.1002/joc.3711.

Herweijer, C., R. Seager, and E. R. Cook, 2006: North American droughts of the mid to late nineteenth century: A history, simulation and implication for Mediaeval drought. *Holocene*, **16**, 159–171, https://doi.org/10.1191/0959683606hl917rp.

Hinkley, D. A., 1977: On quick choice of power transformation. *Appl. Stat.*, **26**, 67–69, https://doi.org/10.2307/2346869.

Hoaglin, D. C., F. Mosteller, and J. W. Tukey, 2000: *Understanding Robust and Exploratory Data Analysis*. John Wiley and Sons, 447 pp.

Hoerling, M., J. Eischeid, J. Perlwitz, X.-W. Quan, K. Wolter, and L. Cheng, 2016: Characterizing recent trends in U.S. heavy precipitation. *J. Climate*, **29**, 2313–2332, https://doi.org/10.1175/JCLI-D-15-0441.1.

Hosking, J. R. M., 1990: L-moments: Analysis and estimation of distributions using linear combinations of order statistics. *J. Roy. Stat. Soc. London*, **52B**, 105–124, https://doi.org/10.1111/j.2517-6161.1990.tb01775.x.

Howard, I. M., and D. W. Stahle, 2020: Tree-ring reconstruction of single-day precipitation totals over eastern Colorado. *Mon. Wea. Rev.*, **148**, 597–612, https://doi.org/10.1175/MWR-D-19-0114.1.

Hu, Q., and S. Feng, 2009: Influence of the Arctic oscillation on central United States summer rainfall. *J. Geophys. Res.*, **115**, D01102, https://doi.org/10.1029/2009JD011805.

Hurrell, J. W., Y. Kushnir, and G. Ottersen, 2003: An overview of the North Atlantic oscillation. *The North Atlantic Oscillation: Climatic Significance and Environmental Impact*, *Geophys. Monogr.*, Vol. 134, Amer. Geophys. Union, 1–35.

Hurvich, C. M., and C. L. Tsai, 1989: Regression and time series model selection in small samples. *Biometrika*, **76**, 297–307, https://doi.org/10.1093/biomet/76.2.297.

Kunkel, K. E., and Coauthors, 2013: Monitoring and understanding trends in extreme storms: State of knowledge. *Bull. Amer. Meteor. Soc.*, **94**, 499–514, https://doi.org/10.1175/BAMS-D-11-00262.1.

LeBlanc, D. C., and D. W. Stahle, 2015: Radial growth responses of four oak species to climate in eastern and central North America. *Can. J. For. Res.*, **45**, 793–804, https://doi.org/10.1139/cjfr-2015-0020.

Marlon, J. R., and Coauthors, 2017: Climatic history of the northeastern United States during the past 3000 years. *Climate Past*, **13**, 1355–1379, https://doi.org/10.5194/cp-13-1355-2017.

McCabe, G. J., M. A. Palecki, and J. L. Betancourt, 2004: Pacific and Atlantic Ocean influences on multidecadal drought frequency in the United States. *Proc. Natl. Acad. Sci. USA*, **101**, 4136–4141, https://doi.org/10.1073/pnas.0306738101.

Meko, D. M., 1981: Applications of Box-Jenkins methods of time-series analysis to reconstruction of drought from tree rings. Ph.D. dissertation, The University of Arizona, 149 pp.

——, and C. H. Baisan, 2001: Pilot study of latewood-width of conifers as an indicator of variability of summer rainfall in the North American monsoon region. *Int. J. Climatol.*, **21**, 697–708, https://doi.org/10.1002/joc.646.

——, E. R. Cook, D. W. Stahle, C. W. Stockton, and M. K. Hughes, 1993: Spatial patterns of tree growth anomalies in the United States and southeastern Canada. *J. Climate*, **6**, 1773–1786, https://doi.org/10.1175/1520-0442(1993)006<1773:SPOTGA>2.0.CO;2.

——, C. W. Stockton, and W. R. Boggess, 1995: The tree-ring record of severe sustained drought. *J. Amer. Water Resour. Assoc.*, **31**, 789–801, https://doi.org/10.1111/j.1752-1688.1995.tb03401.x.

——, D. W. Stahle, D. Griffin, and T. A. Knight, 2011: Inferring precipitation-anomaly gradients from tree rings. *Quat. Int.*, **235**, 89–100, https://doi.org/10.1016/j.quaint.2010.09.006.

Melvin, T. M., and K. R. Briffa, 2008: A ''signal-free'' approach to dendroclimatic standardization. *Dendrochronologia*, **26**, 71–86, https://doi.org/10.1016/j.dendro.2007.12.001.

——, ——, K. Nicolussi, and M. Grabner, 2007: Time-varying-response smoothing. *Dendrochronologia*, **25**, 65–69, https://doi.org/10.1016/j.dendro.2007.01.004.

Mitchell, T. D., and P. D. Jones, 2005: An improved method of constructing a database of monthly climate observations and associated high-resolution grids. *Int. J. Climatol.*, **25**, 693–712, https://doi.org/10.1002/joc.1181.

Mo, K. C., and D. P. Lettenmaier, 2015: Heat wave flash droughts in decline. *Geophys. Res. Lett.*, **42**, 2823–2829, https://doi.org/10.1002/2015GL064018.

Namias, J., 1982: Anatomy of Great Plains protracted heat waves (especially the 1980 U.S. summer drought). *Mon. Wea. Rev.*, **110**, 824–838, https://doi.org/10.1175/1520-0493(1982)110<0824:AOGPPH>2.0.CO;2.

New, M., M. Hulme, and P. Jones, 2000: Representing twentieth-century space–time climate variability. Part II: Development of 1901–96 monthly grids of terrestrial surface climate. *J. Climate*, **13**, 2217–2238, https://doi.org/10.1175/1520-0442(2000)013<2217:RTCSTC>2.0.CO;2.

Newby, P. E., B. N. Shuman, J. P. Donnelly, K. B. Karnauskas, and J. Marsicek, 2014: Centennial-to-millennial hydrologic trends and variability along the North Atlantic Coast, USA, during the Holocene. *Geophys. Res. Lett.*, **41**, 4300–4307, https://doi.org/10.1002/2014GL060183.

Ning, L., and R. S. Bradley, 2016: NAO and PNA influences on winter temperature and precipitation over the eastern United States in CMIP5 GCMs. *Climate Dyn.*, **46**, 1257–1276, https://doi.org/10.1007/s00382-015-2643-9.

Palmer, J. G., and Coauthors, 2015: Drought variability in the eastern Australia and New Zealand summer drought atlas (ANZDA, CE 1500-2012) modulated by the Interdecadal Pacific Oscillation. *Environ. Res. Lett.*, **10**, 124002, https://doi.org/10.1088/1748-9326/10/12/124002.

Palmer, W. C., 1965: Meteorological drought. U.S. Weather Bureau Research Paper 45, 58 pp., http://www.ncdc.noaa.gov/temp-and-precip/drought/docs/palmer.pdf.

Pederson, G. T., and Coauthors, 2011: The unusual nature of recent snowpack declines in the North American cordillera. *Science*, **333**, 332–335, https://doi.org/10.1126/science.1201570.

Pederson, N., A. Bell, E. Cook, U. Lall, N. Devenini, R. Seager, K. Eggleston, and K. Vranes, 2013: Is an epic pluvial masking the water insecurity of the greater New York City region? *J. Climate*, **26**, 1339–1354, https://doi.org/10.1175/JCLI-D-11-00723.1.

Quan, N. T., 1988: The prediction sum of squares as a general measure for regression diagnostics. *J. Bus. Econ. Stat.*, **6**, 501–504, https://doi.org/10.1080/07350015.1988.10509698.

Salzer, M. W., A. G. Bunn, N. E. Graham, and M. K. Hughes, 2014: Five millennia of paleotemperature from tree-rings in the Great Basin, USA. *Climate Dyn.*, **42**, 1517–1526, https://doi.org/10.1007/s00382-013-1911-9.

Schneider, U., A. Becker, P. Finger, A. Meyer-Christoffer, M. Ziese, 2018: GPCC full data monthly product version 2018 at 0.5°: Monthly land-surface precipitation from rain-gauges built on GTS-based and historical data. Global Precipitation Climatology Centre, accessed 15 January 2019, https://doi.org/10.5676/DWD_GPCC/FD_M_V2018_050.

Schulman, E., 1942: Dendrochronology in pines of Arkansas. *Ecology*, **23**, 309–318, https://doi.org/10.2307/1930670.

Seager, R., 2007: The turn of the century North American drought: Global context, dynamics and past analogues. *J. Climate*, **20**, 5527–5552, https://doi.org/10.1175/2007JCLI1529.1.

——, and M. P. Hoerling, 2014: Atmosphere and ocean origins of North American droughts. *J. Climate*, **27**, 4581–4606, https://doi.org/10.1175/JCLI-D-13-00329.1.

——, N. E. Graham, C. Herweijer, A. Gordon, Y. Kushnir, and E. Cook, 2007: Blueprints for Medieval hydroclimate. *Quat. Sci. Rev.*, **26**, 2322–2336, https://doi.org/10.1016/j.quascirev.2007.04.020.

——, N. Pederson, Y. Kushnir, J. Nakamura, and S. Jurburg, 2012: The 1960s drought and subsequent shift to a wetter climate in the Catskill Mountains region of the New York City watershed. *J. Climate*, **25**, 6721–6742, https://doi.org/10.1175/JCLI-D-11-00518.1.

Shoemaker, L. H., 2003: Fixing the *F* test for equal variances. *Amer. Stat.*, **57**, 105–114, https://doi.org/10.1198/0003130031441.

Shuman, B. N., and J. Marsicek, 2016: The structure of Holocene climate change in mid-latitude North America. *Quat. Sci. Rev.*, **141**, 38–51, https://doi.org/10.1016/j.quascirev.2016.03.009.

Smerdon, J. E., B. I. Cook, E. R. Cook, and R. Seager, 2015: Bridging past and future climate across paleoclimatic reconstructions, observations, and models: A hydroclimate case study. *J. Climate*, **28**, 3212–3231, https://doi.org/10.1175/JCLI-D-14-00417.1.

——, and Coauthors, 2017: Comparing proxy and model estimates of hydroclimate variability and change over the Common Era. *Climate Past*, **13**, 1851–1900, https://doi.org/10.5194/cp-13-1851-2017.

Stahle, D. W., and J. S. Dean, 2011: North American tree rings, climatic extremes, and social disasters. *Dendroclimatology: Progress and Prospects*, M. K. Hughes, T. W. Swetnam, and H. F. Diaz, Eds., Developments in Paleoenvironmental Research, Vol. 11, Springer, 297–327.

——, E. R. Cook, M. K. Cleaveland, M. D. Therrell, D. M. Meko, H. D. Grissino-Mayer, E. Watson, and B. H. Luckman, 2000: Tree-ring data document 16th century megadrought over North America. *Eos, Trans. Amer. Geophys. Union*, **81**, 121–132, https://doi.org/10.1029/00EO00076.

——, F. K. Fye, and E. R. Cook, 2007: Tree-ring reconstructed megadroughts over North America since AD 1300. *Climatic Change*, **83**, 133–149, https://doi.org/10.1007/s10584-006-9171-x.

——, and Coauthors, 2009: Cool and warm season precipitation reconstructions over western New Mexico. *J. Climate*, **22**, 3729–3750, https://doi.org/10.1175/2008JCLI2752.1.

——, and Coauthors, 2013: The blue oak woodlands of California: Longevity and hydroclimatic history. *Earth Interact.*, **17**, https://doi.org/10.1175/2013EI000518.1.

——, and Coauthors, 2016: The Mexican Drought Atlas: Tree-ring reconstructions of the soil moisture balance during the late pre-Hispanic, colonial, and modern eras. *Quat. Sci. Rev.*, **149**, 34–60, https://doi.org/10.1016/j.quascirev.2016.06.018.

St. George, S., 2014: An overview of tree-ring width records across the Northern Hemisphere. *Quat. Sci. Rev.*, **95**, 132–150, https://doi.org/10.1016/j.quascirev.2014.04.029.

Swetnam, T. W., C. H. Baisan, A. C. Caprio, P. M. Brown, R. Touchan, R. S. Anderson, and D. J. Hallett, 2009: Multi-millennial fire history of the Giant Forest, Sequoia National Park, California, USA. *Fire Ecol.*, **5**, 120–150, https://doi.org/10.4996/fireecology.0503120.

Therrell, M. D., D. W. Stahle, M. K. Cleaveland, and J. Villanueva-Diaz, 2002: Warm season tree growth and precipitation over Mexico. *J. Geophys. Res.*, **107**, 4205, https://doi.org/10.1029/2001JD000851.

Thom, H. C. S., 1966: Some methods of climatological analysis. WMO Tech. Note 81, 53 pp.

Thompson, D. W. J., and J. M. Wallace, 2001: Regional climate impacts of the Northern Hemisphere annular mode. *Science*, **293**, 85–89, https://doi.org/10.1126/science.1058958.

Tierney, J. E., and Coauthors, 2015: Tropical sea surface temperatures for the past four centuries reconstructed from coral archives. *Paleoceanography*, **30**, 226–252, https://doi.org/10.1002/2014PA002717.

Torbenson, M. C. A., 2019: Cool and warm season climate signals in tree rings from North America. Ph.D. dissertation, University of Arkansas, 132 pp., https://scholarworks.uark.edu/etd/3225/.

——, and D. W. Stahle, 2018: The relationship between cool and warm season moisture over the central United States, 1685–2015. *J. Climate*, **31**, 7909–7924, https://doi.org/10.1175/JCLI-D-17-0593.1.

——, ——, J. Villanueva, E. R. Cook, and D. R. Griffin, 2016: The relationship between earlywood and latewood tree-growth across North America. *Tree-Ring Res.*, **72**, 53–66, https://doi.org/10.3959/1536-1098-72.02.53.

——, ——, I. M. Howard, D. J. Burnette, J. Villanueva-Díaz, E. R. Cook, and D. Griffin, 2019: Multidecadal modulation of the ENSO teleconnection to precipitation and tree growth over subtropical North America. *Paleooceanogr. Paleoclimatol.*, **34**, 886–900, https://doi.org/10.1029/2018PA003510.

USGCRP, 2018: *Impacts, Risks, and Adaptation in the United States*. Vol. II, *Fourth National Climate Assessment*, D. R. Reidmiller et al., Eds., U.S. Global Change Research Program Rep., 1515 pp.

Villanueva-Diaz, J., D. Stahle, B. Luckman, J. Cerano-Paredes, M. Therrell, M. K. Cleaveland, and E. Cornejo-Oviedo, 2007: Winter-spring precipitation reconstruction from tree rings for northeast Mexico. *Climatic Change*, **83**, 117–131, https://doi.org/10.1007/s10584-006-9144-0.

Watson, E., and B. H. Luckman, 2002: The dendroclimatic signal in Douglas-fir and ponderosa pine tree-ring chronologies from the southern Canadian Cordillera. *Can. J. For. Res.*, **32**, 1858–1874, https://doi.org/10.1139/x02-096.

Welsh, C., D. J. Smith, and B. L. Coulthard, 2019: Tree ring records unveil long term influence of the Pacific Decadal Oscillation on snowpack dynamics in the Stikine River basin, northern British Columbia. *Hydrol. Processes*, **33**, 720–736, https://doi.org/10.1002/hyp.13357.

Whan, K., and F. Zwiers, 2017: The impact of ENSO and the NAO on extreme winter precipitation in North America in observations and regional climate models. *Climate Dyn.*, **48**, 1401–1411, https://doi.org/10.1007/s00382-016-3148-x.

Wolter, K., and M. S. Timlin, 2011: El Niño/Southern Oscillation behaviour since 1871 as diagnosed in an extended multivariate ENSO index (MEI.ext). *Int. J. Climatol.*, **31**, 1074–1087, https://doi.org/10.1002/joc.2336.

Woodhouse, C. A., K. E. Kunkel, D. R. Easterling, and E. R. Cook, 2005: The twentieth-century pluvial in the western United States. *Geophys. Res. Lett.*, **32**, L07701, https://doi.org/10.1029/2005GL022413.